The Astrophysical Journal Supplement Series, 268:31 (25pp), 2023 September https://doi.org/10.3847/1538-4365/ace436

The Multiwavelength Environment of Second Bologna Catalog Sources

A. Paggi[1,2], F. Massaro[1,2,3,4], H. Penã-Herazo[1,5,6], V. Missaglia[2,3,7], A. Jimenez-Gallardo[8], F. Ricci[9,10], S. Ettori[11,12], G. Giovannini[8,13], F. Govoni[14], R. D. Baldi[13], B. Mingo[15], M. Murgia[14], E. Liuzzo[13,16], and F. Galati[1]

[1] Dipartimento di Fisica, Università degli Studi di Torino, via Pietro Giuria 1, I-10125 Torino, Italy; alessandro.paggi@unito.it
[2] Istituto Nazionale di Fisica Nucleare, Sezione di Torino, via Pietro Giuria 1, I-10125 Torino, Italy
[3] INAF—Osservatorio Astrofisico di Torino, via Osservatorio 20, I-10025 Pino Torinese, Italy
[4] Consorzio Interuniversitario per la Fisica Spaziale (CIFS), via Pietro Giuria 1, I-10125 Torino, Italy
[5] Instituto Nacional de Astrofísica, Óptica y Electrónica, Tonantzintla, Puebla 72840, Mexico
[6] East Asian Observatory, Hilo, HI 96720, USA
[7] Institute of Astrophysics, Foundation for Research and Technology–Hellas, Voutes, 7110 Heraklion, Greece
[8] Dipartimento di Fisica e Astronomia, Università di Bologna, Via Gobetti 93/2, I-40122 Bologna, Italy
[9] Dipartimento di Matematica e Fisica, Università Roma Tre, via della Vasca Navale 84, I-00146 Roma, Italy
[10] INAF—Osservatorio Astronomico di Roma, Via Frascati 33, I-00040 Monte Porzio Catone, Italy
[11] INAF—Osservatorio di Astrofisica e Scienza dello Spazio di Bologna, via Gobetti 93/3, I-40129 Bologna, Italy
[12] Istituto Nazionale di Fisica Nucleare, Sezione di Bologna, viale Berti Pichat 6/2, I-40127 Bologna, Italy
[13] INAF—Istituto di Radioastronomia (IRA), Via P. Gobetti 101, I-40129 Bologna, Italy
[14] INAF—Osservatorio Astronomico di Cagliari, Via della Scienza 5, I-09047 Selargius, Italy
[15] School of Physical Sciences, The Open University, Walton Hall, Milton Keynes, MK7 6AA, UK
[16] Italian Alma Regional Center (ARC), Via Piero Gobetti 101, I-40129 Bologna, Italy
Received 2023 February 18; revised 2023 June 22; accepted 2023 July 3; published 2023 September 7

Abstract

We present the first results of the Chandra Cool Targets (CCT) survey of the Second Bologna Catalog (B2CAT) of powerful radio sources, aimed at investigating the extended X-ray emission surrounding these sources. For the first 33 sources observed in the B2CAT CCT survey, we performed both imaging and spectral X-ray analysis, producing multiband Chandra images, and compared these images with radio observations. To evaluate the presence of extended emission in the X-rays, we extracted surface flux profiles comparing them with simulated ACIS point-spread functions. We detected X-ray nuclear emission for 28 sources. In addition, we detected eight regions of increased X-ray flux originating from radio hot spots or jet knots, and a region of decreased flux, possibly associated with an X-ray cavity. We performed X-ray spectral analysis for 15 nuclei and found intrinsic absorption significantly larger than the Galactic values in four of them. We detected significant extended X-ray emission in five sources, and fitted their spectra with thermal models with gas temperatures $\sim$2 keV. In the case of B2.1 0742+31, the surrounding hot gas is compatible with the intracluster medium of low-luminosity clusters of galaxies, while the X-ray diffuse emission surrounding the highly disturbed wide-angle-tailed radio galaxy B2.3 2254+35 features a luminosity similar to those of relatively bright galaxy groups, although its temperature is similar to those of low-luminosity galaxy clusters. These results highlight the power of low-frequency radio selection, combined with short Chandra snapshot observations, for investigating the properties of X-ray emission from radio sources.

Unified Astronomy Thesaurus concepts: Active galaxies (17); Galaxy jets (601); Galaxy clusters (584)

Supporting material: figure set

1. Introduction

Diffuse X-ray emission associated with radio sources extending well beyond their host galaxies up to scales of hundreds of kiloparsecs has been known and observed since the first X-ray Uhuru (e.g., Gursky et al. 1971) and Einstein (e.g., Jones et al. 1979) missions, and more recently with the XMM-Newton (e.g., Gobat et al. 2011) and Chandra (e.g., Maselli et al. 2018) telescopes (see also Fabian et al. 2003; Scharf et al. 2003; Erlund et al. 2006; Evans et al. 2006).

In the last few decades, the Chandra telescope has extensively studied the X-ray emission of high-redshift radio galaxies, often used as tracers of galaxy clusters with poor or moderately rich environments (see, e.g., Worrall 2002; Crawford & Fabian 2003; Worrall 2009; Golden-Marx et al. 2021), since extended X-ray emission from these sources can be due to the thermal radiation arising from the hot gas trapped by the gravitational attraction of giant galaxies or permeating the intergalactic medium (see, e.g., Fabian et al. 2001; Ineson et al. 2013, 2015).

Alternatively, when the extended X-ray emission in these sources shows a general alignment with the radio axis and/or is spatially coincident with radio structures, a significant contribution to its flux is expected to come from nonthermal processes, and in particular from inverse Compton (IC) scattering of the radio-emitting electrons. In radio lobes, the X-ray emission is generally interpreted as due to the IC scattering of these electrons on cosmic microwave background (CMB) photons permeating the radio lobes (IC/CMB; Hoyle 1965; Bergamini et al. 1967; Okoye 1972, 1973; Harris & Grindlay 1979; Schwartz et al. 2000; Tavecchio et al. 2000; Meyer et al. 2019; Breiding et al. 2023), while in radio hot spots the X-ray emission is believed to be dominated by synchrotron self-

Compton radiation (Kataoka & Stawarz 2005), that is, the IC scattering of synchrotron photons by electrons in the radio jets that emitted the synchrotron photons in the first place (Hardcastle et al. 2004). Finally, X-ray emission in radio galaxies on ∼100–200 kpc scales can also be significantly contributed by IC scattering from far-IR photons in galactic starbursts (Smail et al. 2009, 2012).

To investigate the nature of the extended X-ray emission surrounding radio sources and study their evolution, in the last decade we have carried out a Chandra snapshot survey of the revised Third Cambridge Catalogue (3CR; Bennett 1962; Spinrad et al. 1985) to obtain X-ray coverage of the entire catalog (Massaro et al. 2010, 2012, 2015). Through this observational program, we found X-ray emission associated with radio jets (see, e.g., Massaro et al. 2009) and hot spots (see, e.g., Massaro et al. 2011; Orienti et al. 2012) as well as diffuse X-ray emission from hot atmospheres and the intracluster medium (ICM) in galaxy clusters (see, e.g., Hardcastle et al. 2010, 2012; Dasadia et al. 2016; Ricci et al. 2018; Missaglia et al. 2021), extended X-ray emission aligned with the radio axis of several moderate- and high-redshift radio galaxies (see, e.g., Massaro et al. 2013, 2018; Stuardi et al. 2018; Jimenez-Gallardo et al. 2020, 2021; Paggi et al. 2021), and extended X-ray emission spatially associated with optical emission line regions not coincident with radio structures (Massaro et al. 2009; Balmaverde et al. 2012; Jimenez-Gallardo et al. 2022).

In this work we present the first results from a Chandra snapshot survey performed on the Second Bologna Catalog (B2CAT) of powerful radio sources. The B2CAT (Colla et al. 1970, 1972, 1973; Fanti et al. 1974), listing about 10,000 sources detected above 0.1 Jy (completeness above 0.2 Jy) at 408 MHz with the Bologna Northern Cross Telescope between 21° and 40° decl., is well suited for studying the properties of extragalactic radio sources. As it is a low-frequency radio selected sample, its selection criteria are unbiased with respect to X-rays and active galactic nucleus (AGN) viewing angles. This catalog has been the source of well-studied samples of radio-loud active galaxies (Fanti et al. 1987), as well as radio-loud quasars (Rogora et al. 1986) and spiral galaxies (Gioia & Gregorini 1980). The high sensitivity of the B2CAT with respect to other radio samples, e.g., the 3CR, has allowed us to study the properties of low-luminosity radio galaxies, such as Fanaroff–Riley I (FRI; Fanaroff & Riley 1974) radio galaxies, and the nonthermal properties of spiral galaxies and low-luminosity quasars.

In addition, the B2CAT spans a wide range of redshift and radio power, and it is augmented by a vast suite of ground- and space-based observations at all accessible wavelengths (optical: Capetti et al. 2002; de Ruiter et al. 2002; radio band between 1.4 and 8 GHz: Fanti et al. 1974; Harris et al. 1980; Padrielli et al. 1981; Law-Green et al. 1995). This catalog represents an ideal sample with which to study the X-ray emission arising from jet knots, hot spots, and nuclei of radio sources; look for new galaxy clusters via the presence of extended X-ray emission unrelated to the radio structures (Belsole et al. 2007; Mannering et al. 2013); and investigate observational evidence of AGN feedback with the hot gas in galaxies and in groups and clusters of galaxies (Fabian 2012; Kraft et al. 2012; Mingo et al. 2017). The B2CAT therefore represents a powerful tool with which to optimize the Chandra Cool Targets (CCT[17]) observing strategy, that is, observations acquired while the spacecraft performs pointings to avoid overheating (or excessive cooling) of various observatory subsystems.

The paper is organized as follows. A brief description of the B2CAT CCT sources observed to date is presented in Section 2. Chandra data reduction and analysis are presented in Section 3. Results on individual sources' imaging and spectral analysis are presented in Sections 3.1, 3.2, and 3.3, while Section 4 is devoted to our conclusions. Unless otherwise stated we adopt cgs units for numerical results and we also assume a flat cosmology with $H_0 = 69.6\,\mathrm{km\,s^{-1}\,Mpc^{-1}}$, $\Omega_M = 0.286$, and $\Omega_\Lambda = 0.714$ (Bennett et al. 2014).

2. Sample Description

In the selection of B2CAT CCT survey targets we started from B2CAT excluding sources already observed by Chandra. Taking into account the ecliptic latitude cut ($\ell > 55°$), we then selected a sample of 3080 sources. We stress that, due to the serendipitous nature of the CCT program, large samples are required to perform such observations, and that the proposed sources will be observed randomly. Finally, for this survey we applied for snapshot (16 ks) observations, following the same approach used for the Chandra 3CR survey (Massaro et al. 2010).

The sample of radio sources discussed in this work is constituted by the first 33 B2CAT targets observed by Chandra during the CCT survey up to 2023 June. The main properties of these sources are presented in Table 1. Redshift measurements are available for only seven sources.

In addition to the newly obtained Chandra data, we collected multiwavelength radio data for the sources in the sample. In particular, to investigate the correlation between the diffuse X-ray emission and the extended radio structures, we collected 74 MHz Karl G. Jansky Very Large Array (VLA) data obtained through the VLA Low-frequency Sky Survey Redux (VLSSr; Lane et al. 2014),[18] 145 MHz Low Frequency Array (LOFAR; van Haarlem et al. 2013) observations from the forthcoming Data Release 2 (DR2) of LoTSS[19] processed by the international LOFAR collaboration as part of LOFAR Data Release 1 and 2 (Shimwell et al. 2017, 2019, 2022; Tasse et al. 2021), 150 MHz Giant Metrewave Radio Telescope (GMRT) data obtained from the TIFR GMRT Sky Survey (TGSS; Intema et al. 2017),[20] 1.4 GHz VLA data obtained through the NRAO VLA Sky Survey (NVSS; Condon et al. 1998),[21] and 3 GHz VLA data obtained through the VLA Sky Survey (VLASS; Lacy et al. 2020).[22]

In the Appendix we report the complete set of radio images (see Figure 13) available in the aforementioned surveys for the B2CAT sources considered here, together with estimates of the radio flux for different radio structures (see Table A1).

[17] https://cxc.harvard.edu/proposer/CCTs.html

[18] VLSSr images cover an area of ∼30,530 deg^2 with a resolution of 75″, and an rms of ∼0.1 Jy beam^{-1}.

[19] DR2 v2.2 was run as part of the ddf pipeline (https://github.com/mhardcastle/ddf-pipeline). LoTSS DR1 consists of images at 6″ resolution and ∼70 μJy beam^{-1} sensitivity covering an area of ∼400 deg^2 while the footprint of DR2 covers an area of approximately 5700 deg^2; both surveys were performed in the northern hemisphere.

[20] TGSS images cover an area of ∼36,900 deg^2, and have a resolution of 25″ for decl. >19° and of 25″/cos (decl.−19°) for decl. <19°, with a median rms of ∼3.5 mJy beam^{-1}.

[21] NVSS images cover the entire north sky above −40° decl. with a resolution of 45″, and an rms of ∼450 μJy beam^{-1}.

[22] VLASS images cover an area of ∼33,885 deg^2 with decl. > −40° with a resolution of 2.″5, with an rms of ∼120 μJy beam^{-1} for the single-epoch observations and of ∼70 μJy beam^{-1} for the three combined epochs.

Table 1
Main Properties of the Radio Sources Investigated in the Present Work

Source Name	R.A. (hh:mm:ss.ss)	Decl. (dd:mm:ss.s)	z	Chandra OBSID	Clean Exp. (ks)	Nuclear $F_{0.3-7\ \mathrm{keV}}$ (10^{-13} erg cm^{-2} s^{-1})	Nuclear $L_{0.3-7\ \mathrm{keV}}$ (erg s^{-1})	Extended $F_{0.3-3\ \mathrm{keV}}$ (10^{-13} erg cm^{-2} s^{-1})	Extended $L_{0.3-3\ \mathrm{keV}}$ (erg s^{-1})	Radio Morph.	Bin Size	Smoothing
B2.4 0004+21	00:07:26.69	+22:03:23.8	...	26155	15.9	$1.95^{+0.15}_{-0.15}$	...	$0.45^{+0.19}_{-0.18}$	...	FRII	2	4
B2.2 0038+25B	00:41:18.54	+25:49:50.9	...	27884	14.6	$0.05^{+0.03}_{-0.02}$	...	<0.06	...	FRII	2	3
B2.2 0143+24	01:46:28.83	+25:06:04.6	...	23074	15.3	$0.06^{+0.04}_{-0.03}$	...	<0.08	...	FRII	4	4
B2.4 0145+22	01:47:49.84	+22:38:55.0	...	27519	15.9	$0.79^{+0.10}_{-0.10}$	...	<0.32	...	FRII	4	3
B2.4 0229+23	02:32:20.96	+23:17:24.6	3.420	27538	14.9	$5.81^{+0.29}_{-0.29}$	$6.4^{+0.3}_{-0.3} \times 10^{46}$	$0.61^{+0.35}_{-0.34}$	$6.7^{+3.9}_{-3.7} \times 10^{45}$	Compact	2	3
B2.1 0241+30	02:44:42.80	+30:20:44.5	...	26174	15.4	$0.05^{+0.03}_{-0.02}$	...	$0.23^{+0.11}_{-0.11}$	...	FRII	2	6
B2.1 0302+31	03:05:23.16	+31:29:42.5	...	26198	15.9	...	...	$3.14^{+0.39}_{-0.39}$	...	HyMoR	2	8
B2.4 0401+23	04:04:51.68	+24:07:02.3	...	26199	15.9	$0.42^{+0.08}_{-0.07}$	...	<0.05	...	FRII	2	5
B2.2 0410+26	04:13:23.64	+26:48:47.5	...	26200	15.9	$0.11^{+0.04}_{-0.03}$	...	$0.13^{+0.13}_{-0.13}$	...	Compact	2	5
B2.4 0412+23	04:15:12.82	+23:47:52.3	...	26214	15.9	$2.69^{+0.18}_{-0.18}$	...	$0.39^{+0.23}_{-0.22}$	...	Lobes	2	5
B2.3 0454+35	04:58:07.36	+35:45:46.3	...	27589	15.8	$8.00^{+0.35}_{-0.34}$	...	<0.67	...	One-sided jet	1	3
B2.1 0455+32B	04:59:05.74	+32:36:30.0	...	27590	15.9	$0.08^{+0.04}_{-0.03}$	...	<0.12	...	Lobes	2	4
B2.1 0455+32C	04:59:14.08	+32:26:11.4	...	27591	15.9	$0.07^{+0.04}_{-0.03}$	...	<0.11	...	FRII	2	4
B2.3 0516+40	05:19:45.53	+40:15:44.5	...	27750	14.9	$0.04^{+0.04}_{-0.03}$	...	<0.25	...	Compact	4	3
B2.1 0536+33B	05:40:03.88	+33:42:04.2	...	22192	15.9	$0.28^{+0.07}_{-0.06}$	...	<0.09	...	FRII	1	4
B2.1 0549+29	05:52:55.28	+29:33:07.9	...	26230	15.9	$0.65^{+0.11}_{-0.10}$	...	$0.33^{+0.26}_{-0.25}$	...	Lobes	1	3
B2.1 0643+30	06:46:15.48	+30:41:16.0	...	26263	15.8	$0.80^{+0.10}_{-0.10}$	...	$0.30^{+0.16}_{-0.16}$	...	Compact	1	3
B2.1 0742+31	07:45:41.63	+31:43:10.3	0.461	26264	15.9	$21.90^{+0.50}_{-0.50}$*	$17.7^{+0.4}_{-0.4} \times 10^{44}$	$1.82^{+0.47}_{-0.47}$	$1.5^{+0.4}_{-0.4} \times 10^{44}$	FRII	2	8
B2.2 0755+24	07:58:02.75	+24:21:58.1	0.502	26265	15.9	$0.08^{+0.04}_{-0.03}$	$7.9^{+4.0}_{-3.0} \times 10^{42}$	$0.17^{+0.14}_{-0.14}$	$1.7^{+1.4}_{-1.4} \times 10^{43}$	Lobes	2	5
B2.3 0848+34	08:51:08.44	+34:19:20.4	0.697	27850	14.8	$0.09^{+0.04}_{-0.03}$	$1.9^{+0.9}_{-0.7} \times 10^{43}$	<0.12	$<2.6 \times 10^{43}$	Lobes	2	4
B2.4 0939+22A	09:41:55.62	+21:48:47.8	0.572	26291	15.7	$0.09^{+0.04}_{-0.03}$	$1.2^{+0.5}_{-0.4} \times 10^{43}$	$0.34^{+0.15}_{-0.14}$	$4.6^{+12.0}_{-1.9} \times 10^{43}$	FRII	2	6
B2.4 1112+23	11:15:04.89	+23:25:50.2	...	26333	15.3	$0.06^{+0.04}_{-0.03}$	...	<0.12	...	Compact	2	6
B2.3 1234+37	12:36:50.64	+36:55:30.1	...	27609	15.9	$0.13^{+0.05}_{-0.04}$	...	<0.22	...	Lobes	2	3
B2.2 1334+27	13:36:41.37	+27:03:43.7	3.228	27617	15.9	$0.92^{+0.10}_{-0.10}$	$8.8^{+1.0}_{-1.0} \times 10^{45}$	<0.13	$<1.2 \times 10^{45}$	Lobes	2	4
B2.2 1338+27	13:40:29.96	+27:22:14.6	...	27618	16.9	<0.09	...	<0.04	...	Lobes	4	3
B2.2 1439+25	14:42:04.09	+25:03:30.0	...	27411	15.9	...	...	$0.14^{+0.14}_{-0.14}$	...	Lobes	4	5
B2.4 1512+23	15:14:15.01	+23:28:53.2	0.088	27718	14.9	$0.16^{+0.05}_{-0.05}$	$3.1^{+1.0}_{-1.0} \times 10^{41}$	$0.10^{+0.08}_{-0.07}$	$2.0^{+1.6}_{-1.4} \times 10^{41}$	FRII	2	6
B2.4 2054+22B	20:56:57.55	+22:30:11.7	...	27821	15.9	$0.06^{+0.04}_{-0.03}$	...	<0.11	...	FRII	2	5
B2.2 2104+24	21:06:21.19	+24:33:22.7	...	22170	16.4	$3.01^{+0.18}_{-0.17}$	...	<0.29	...	FRII	1	3
B2.2 2133+27	21:35:17.61	+27:16:14.1	...	26149	15.9	...	...	$0.18^{+0.15}_{-0.15}$	...	Lobes	1	6
B2.3 2254+35	22:56:46.03	+35:40:56.8	0.114	22193	15.9	$0.10^{+0.04}_{-0.03}$	$3.4^{+1.4}_{-1.0} \times 10^{41}$	$6.75^{+0.65}_{-0.62}$	$2.3^{+0.2}_{-0.2} \times 10^{43}$	WAT	4	6
B2.2 2328+26	23:30:34.44	+27:05:21.2	...	26122	15.9	$0.12^{+0.04}_{-0.04}$	...	<0.05	...	Compact	1	4
B2.3 2334+39	23:36:55.64	+40:06:06.5	...	26342	15.9	<0.05	...	<0.11	...	FRI	2	6

Notes. In the table we list the source's B2CAT name (Source Name), its J2000 coordinates (R.A. and Decl.) and redshift (z), the Chandra OBSID, the net exposure after filtering for time intervals of high background flux (Clean Exp.), the intrinsic 0.3–7 keV nuclear flux estimated assuming a power-law spectrum with a 1.8 slope (Nuclear $F_{0.3-7\ \mathrm{keV}}$) and the corresponding nuclear luminosity for sources with available redshift (Nuclear $L_{0.3-7\ \mathrm{keV}}$), the intrinsic 0.3–3 keV extended emission flux estimated assuming a thermal spectrum with 2 keV temperature and 0.25 solar abundance (Extended $F_{0.3-3\ \mathrm{keV}}$) and the corresponding extended emission luminosity for sources with available redshift (Extended $L_{0.3-3\ \mathrm{keV}}$), the general radio morphology (Radio Morph.), the image pixel size in terms of the native ACIS pixel size (Bin Size), and the σ width of the smoothing Gaussian kernel expressed in image pixels (Smoothing) used in Figures 1, 5, and 10. The flux marked with an asterisk (*) was extracted from a nuclear region affected by significant pileup.

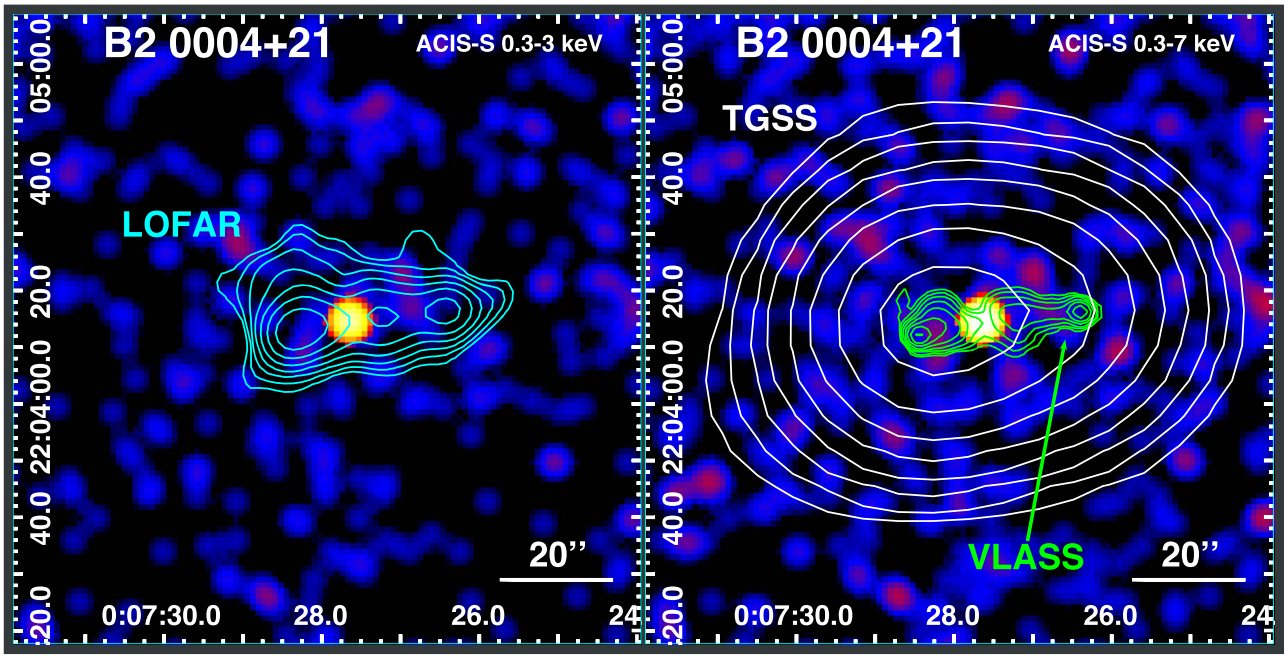

Figure 1. Chandra ACIS-S flux maps (0.3–3 keV and 0.3–7 keV band images on the left and on the right, respectively). Radio map contours are overlaid in cyan (LOFAR 145 MHz), white (TGSS 150 MHz), and green (VLASS 3 GHz). The radio contours start at 10 times the rms level, increasing by factors of 2. The complete figure set (33 images) is available in the online journal.

(The complete figure set (33 images) is available.)

3. Data Analysis

Chandra observations of B2CAT sources were retrieved from the Chandra Data Archive through the ChaSeR service[23] (see Table 1). They consist of ACIS-S snapshot observations with nominal exposure time of 16 ks, performed between 2019 April and 2023 June in VFAINT mode. These data have been analyzed with the Chandra Interactive Analysis of Observations (CIAO; Fruscione et al. 2006) data analysis system version 4.14 and the Chandra Calibration Database (CALDB) version 4.9.8, adopting standard procedures. The observations were filtered for time intervals of high background flux exceeding 3σ above the average level with the DEFLARE task, to attain the final exposures listed in Table 1. Field point sources in the 0.3–7 keV energy band were detected with the WAVDETECT task, adopting a $\sqrt{2}$ sequence of wavelet scales (i.e., 1, 1.41, 2, 2.83, 4, 5.66, 8, 11.31, and 16 pixels) and a false-positive probability threshold of 10^{-6}. Given the relatively short exposure times and the consequent low statistics, we did not correct the absolute astrometry of the Chandra ACIS-S images and did not register them to radio maps, as the typical shift for Chandra images found during the 3CR Chandra Snapshot Survey is $0\farcs5$ (see, e.g., Massaro et al. 2011; Jimenez-Gallardo et al. 2020).

We produced broadband (0.3–7 keV), soft-band (0.3–3 keV), and hard-band (3–7 keV) Chandra images centered on ACIS-S chip 7. We also produced point-spread function (PSF) maps (with the MKPSFMAP task), effective area corrected exposure maps, and flux maps (using the FLUX_OBS task; see Figure 1). The image pixel sizes and the σ widths of the Gaussian kernel used for smoothing are listed in Table 1.

[23] http://cda.harvard.edu/chaser

3.1. Imaging Analysis

We first proceeded to searching for nuclear detections in the broad 0.3–7 keV band images. Using the higher-resolution VLASS data, we defined $2''$ circular regions coincident with the core emission as identified in the VLASS images. If source cores were not clearly detected in the VLASS images, we tentatively identified as source cores those compact X-ray regions lying at the center of the radio structures (see Section 3.2). We evaluated the nuclear X-ray fluxes by making use of the CIAO SRCFLUX task, which evaluates the PSF corrections and the detector effective area and response function at the source location, assuming a power-law spectrum with a 1.8 slope—as usually observed in AGN nuclear emission—and taking into account the photoelectric absorption by the Galactic column density along the line of sight (HI4PI Collaboration et al. 2016). The nuclear fluxes are listed in Table 1.

With this procedure, we confirmed nuclear detections for 28 out of 33 sources, with 19 being detected at least at 3σ significance. For seven other sources (B2.2 0143+24, B2.1 0241+30, B2.1 0455+32B, B2.1 0455+32C, B2.2 0775+24, B2.4 1112+23, and B2.4 2054+22B) we obtained a 2σ significance detection of nuclear emission, for two sources (B2.3 0516+40 and B2.2 0038+25B) we obtained a marginal 1σ significance detection of nuclear emission, and for another two sources (B2.2 1338+27 and B2.3 2334+39) we were only able to put a 1σ upper limit on the nuclear flux. For the remaining three sources (B2.1 0302+31, B2.2 1439+25, and B2.2 2133+27), since we do not have any clear indication—neither in radio nor in X-ray data—of the location of the core, we do not report any nuclear flux estimate. We note that the brightest nucleus in our sample, B2.1 0742+31, is significantly affected by pileup, as shown in the map obtained with the CIAO

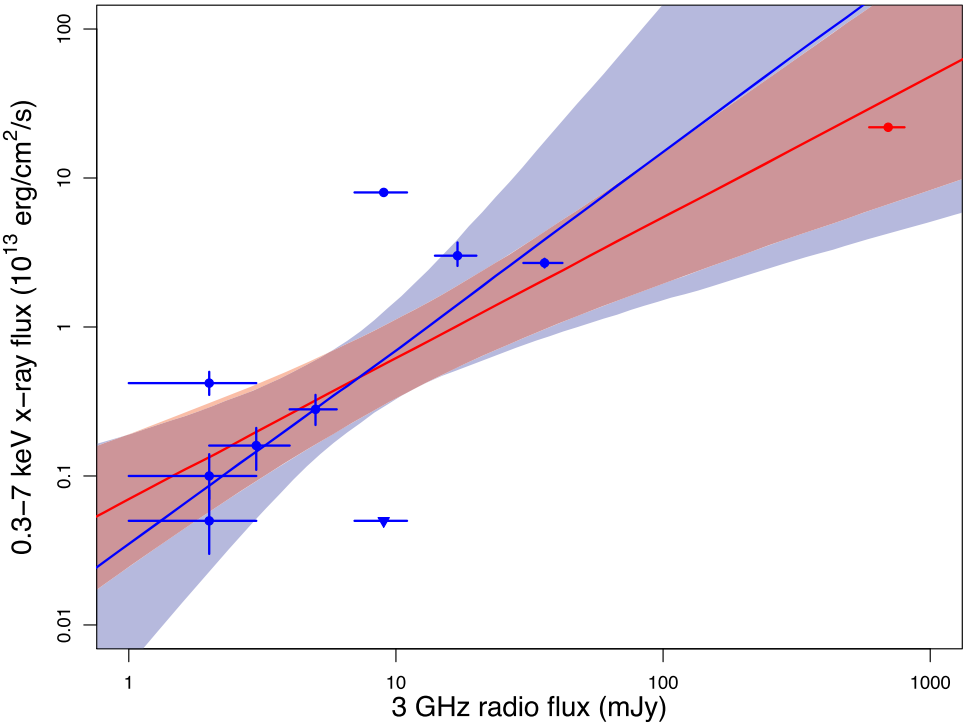

Figure 2. X-ray 0.3–7 keV nuclear fluxes vs. 3 GHz radio nuclear specific fluxes for the sources for which both estimates are available (see Section 3.1). Upper limits on X-ray fluxes are represented with triangles pointing down. The red line indicates the linear regression to the logarithmic data that include the highly piled-up source B2.1 0742+31 (indicated with a red circle), while the light red shaded area represents the 1σ uncertainty around the best-fit relation. The blue line and light blue shaded area represent the linear regression and uncertainty for the logarithmic data that exclude B2.1 0742+31.

task PILEUP_MAP, and therefore the value of $17.7 \pm 0.4 \times 10^{-13}$ erg cm^{-2} s^{-1} reported in Table 1 should be considered as a lower limit to the real flux (see Section 3.3).

The correlation between AGN nuclear radio and X-ray emission from the ROSAT All Sky Survey (Voges et al. 1999) has been observed and discussed in several works (e.g., Worrall & Birkinshaw 1994; Zuther et al. 2012). To investigate this correlation in our sample, in Figure 2 we plot the X-ray nuclear fluxes evaluated above versus the 3 GHz radio nuclear specific fluxes, evaluated from VLASS maps that show a discernible nuclear emission (region N in Table A1). Despite the paucity of the sample, there appears to be a correlation between the nuclear emission at radio and X-ray frequencies, as evaluated through hierarchical Bayesian linear regression (Kelly 2007). In particular, a linear regression of the logarithmic values of both quantities including the highly piled-up B2.1 0742+31 yields a slope of $0.95^{+0.36}_{-0.35}$ with a correlation coefficient of 0.75 (red line in Figure 2), while excluding it yields a slope of $1.31^{+0.83}_{-0.81}$ with a correlation coefficient of 0.65 (blue line in Figure 2), both consistent with previous results on radio-loud AGNs (e.g., Brinkmann et al. 1997, 2000). We note that the X-ray fluxes expected from the correlation that excludes B2.1 0742+31 lie at larger values than that evaluated for this source, reinforcing the point that the X-ray flux evaluated for B2.1 0742+31 should be regarded as a lower limit.

As shown in Figure 1, many sources in the present sample show hints of diffuse soft X-ray 0.3–3 keV band emission associated with the extended radio structures mapped by the GMRT and LOFAR images. In order to get a preliminary characterization of this diffuse emission we evaluated its flux by making use of the CIAO SRCFLUX task, assuming a thermal spectrum with 2 keV temperature and 0.25 solar abundance—as expected from typical ICM emission—and taking again into account the Galactic photoelectric absorption. The fluxes of the extended emission are listed in Table 1.

Also the correlation between radio and X-ray diffuse emission in clusters has been discussed in several studies (e.g., Parekh et al. 2017; van Weeren et al. 2019). To investigate this in our sample, in Figure 3 we plot these X-ray fluxes versus the 145 MHz specific fluxes evaluated from LOFAR maps from regions of extended radio emission (regions A and B listed in Table A1). In this case, however, the correlation between the extended emission at radio and X-ray frequencies appears very low, with a slope of $0.20^{+0.36}_{-0.38}$ and a correlation coefficient of 0.26.

To evaluate the significance of this extended emission in X-rays, we extracted net surface flux profiles in the 0.3–3 keV band from concentric annuli centered on the radio core positions, excluding counts from detected sources, and evaluating the background level from source-free regions of chip 7. The width of the bins was adaptively determined to reach a minimum signal-to-noise ratio of 3. In the outer regions, when this ratio could not be reached, we extended the bin width to the edges of the ACIS chip.

We then compared these profiles with those extracted from simulated ACIS PSFs, using the same procedure fully described in Fabbiano et al. (2020) and briefly summarized here. The Chandra PSFs were simulated using rays produced by the Chandra Ray Tracer (ChaRT[24]) projected on the image plane by MARX.[25] For each observation, we generated the average from 1000 PSF simulations centered at the coordinates of the radio or X-ray cores. We then produced images of these PSFs in the 0.3–3 keV band, and extracted profiles from the

[24] http://cxc.harvard.edu/ciao/PSFs/chart2/
[25] http://space.mit.edu/CXC/MARX/

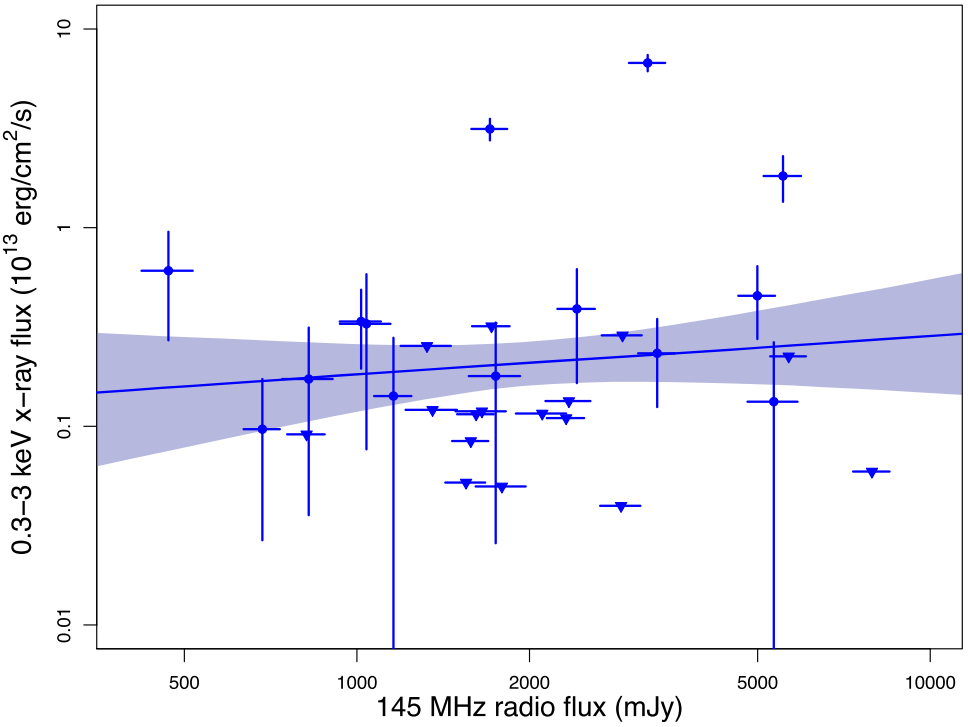

Figure 3. X-ray 0.3–3 keV extended emission fluxes vs. 145 MHz specific fluxes of the extended radio structures (see Section 3.1). Upper limits on X-ray fluxes are represented with triangles pointing down. The blue line indicates the linear regression to the logarithmic data, while the light blue shaded area represents the 1σ uncertainty around the best-fit relation.

same annuli used for the source images. Finally, the PSF surface flux profiles were normalized to match the level obtained in the innermost annulus for the source images.

We found that the 0.3–3 keV soft-band emission is extended at least at 5σ significance beyond $10''$ for five sources in the present sample (B2.4 0004+21, B2.1 0302+31, B2.4 0412 +23, B2.1 0742+31, and B2.3 2254+35). Figure 4 shows the comparison of the net surface flux profiles for these sources (black dots) and their corresponding PSFs (red dots), and we see that the former are clearly extended above the latter, especially for B2.1 0302+31 and B2.3 2254+35.

3.2. Individual Sources

In this section, we report X-ray compact features associated with radio structures of the sources in our sample, while properties of the extended X-ray emission will be discussed in Section 3.3. The broadband 0.3–7 keV flux maps of the central region of each source are presented in Figure 5, with the 3 GHz VLASS contours from Figure 1 overlaid in black.

3.2.1. B2.4 0004+21

Also known as NVSS J000727+220413, this source shows a typical Fanaroff–Riley II (FRII; Fanaroff & Riley 1974) structure, with indication of extended X-ray emission (see Figure 4). Apart from the bright X-ray nucleus (region 1 in Figure 5, with a 0.3–7 keV flux of $20^{+2}_{-2} \times 10^{-14}$ erg cm^{-2} s^{-1}; see Section 3.1), the regions of increased X-ray flux in correspondence with the radio structures (regions 2 and 3 in Figure 5) have low ($<2\sigma$) significance with respect to the level of the diffuse emission at the same radial distance from the nucleus.

3.2.2. B2.2 0038+25B

This source, also known as PKS 0038+255, shows an FRII radio morphology as mapped by the VLASS image. We do not have a clear detection of the radio core, although between the lobes we see a faint region of X-ray emission (region 1 in Figure 5) with a 0.3–7 keV flux of $5^{+3}_{-2} \times 10^{-15}$ erg cm^{-2} s^{-1} (see Section 3.1), which we identify as the X-ray nucleus. There are some hints about this region extending along the radio axis toward the lobes, but the low statistic prevents us from drawing further conclusions.

3.2.3. B2.2 0143+24

This source, also known as NVSS J014628+250616, shows a complex, extended radio morphology in LOFAR images, while VLASS data indicate a typical FRII structure (see Figure 1). In Figure 5, region 1 indicates the location of the possible source nucleus. This region yields an upper limit on the flux of $6^{+4}_{-3} \times 10^{-15}$ erg cm^{-2} s^{-1} (see Section 3.1). On both sides of region 1, along the radio axis, there are two regions of increased flux in front of the hot spots (regions 2 and 3). The brightest region 2 has 12 broadband counts, and by sampling the emission at the same radial distance from the putative nucleus we can conclude that this is marginally significant at the 3σ level.

3.2.4. B2.4 0145+22

This source, known as NVSS J014750+223852, shows in the VLASS image an FRII structure, without indications of a clearly detected radio core. In Figure 5, we indicate with region 1 the position of a bright X-ray source between the two radio jets that we identify as the nucleus, for which we estimated a

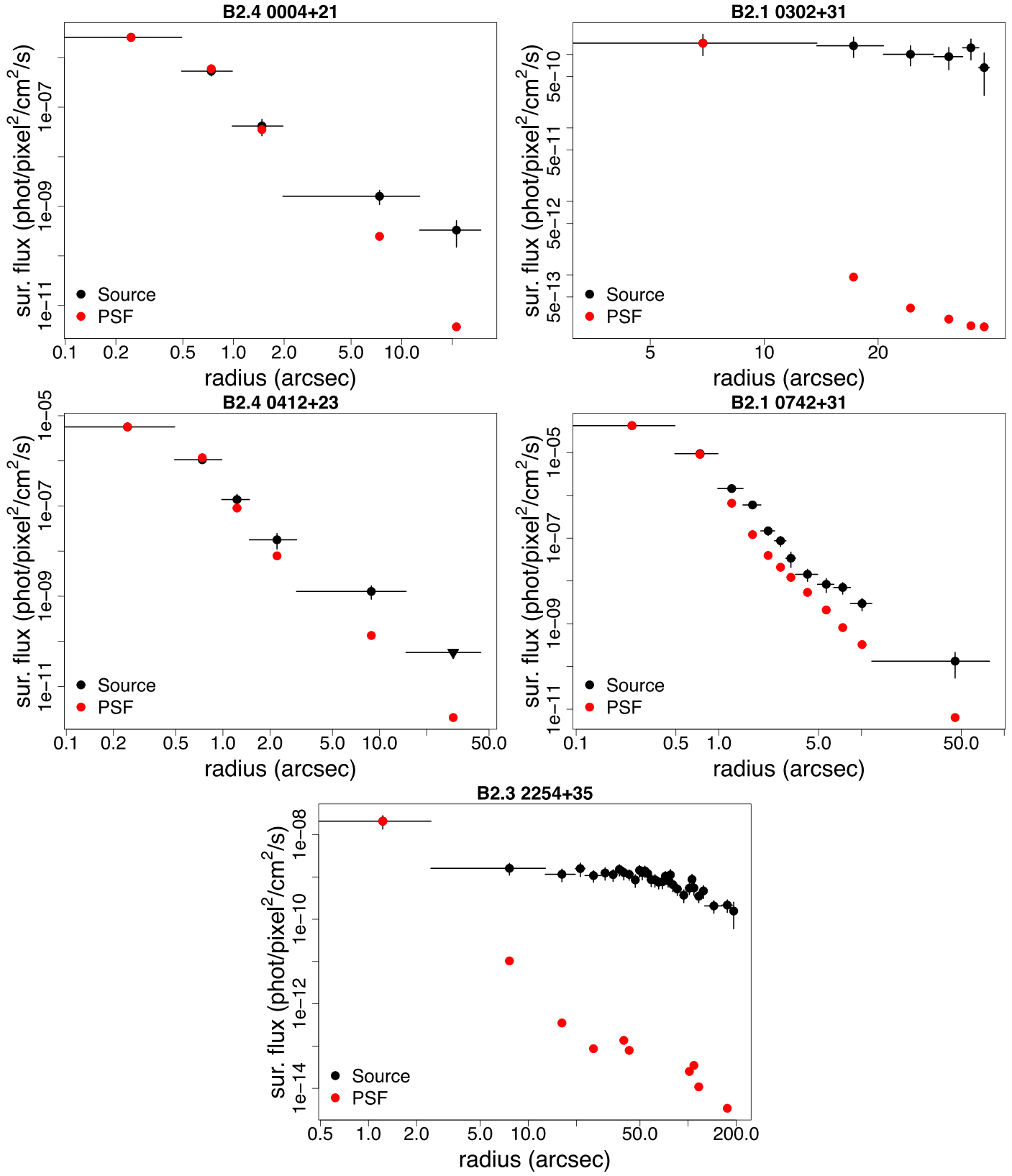

Figure 4. Surface flux profiles for the sources that show evidence of extended X-ray emission in the soft 0.3–3 keV band (see Section 3.1). For each source we present with black dots the surface flux profiles from the source itself, and with red dots the profiles from the simulated PSF.

broadband flux of $8^{+1}_{-1} \times 10^{-14}$ erg cm^{-2} s^{-1} (see Section 3.1). On the east side of the nucleus there is a region of increased X-ray flux co-spatial with the eastern radio jet (region 2), possibly connected with a jet knot. This region contains 12 broadband counts, significant at the 4σ level above the emission at the same radial distance from the nucleus.

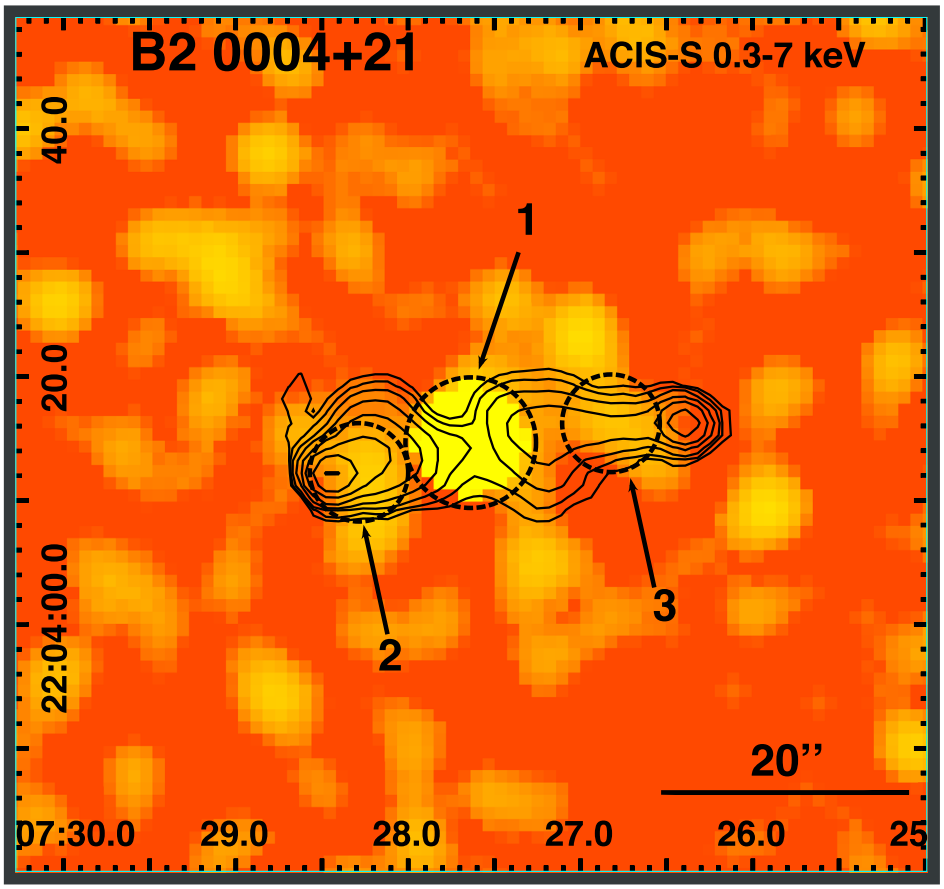

Figure 5. Chandra ACIS-S 0.3–7 keV flux maps of the central region of the sources in the present sample. In each panel we overlay in black the 3 GHz VLASS contours from Figure 1. The black dashed circles mark the regions discussed in detail in Section 3.2. For sources B2.1 0302+31, B2.1 0742+31, and B2.3 2254+35 the white ellipse shows the extraction region used for the spectral fittings presented in Table 4, while the blue ellipse shows the region of radio emission excluded in the spectral fittings presented in Table 5. The complete figure set (33 images) is available in the online journal.

(The complete figure set (33 images) is available.)

3.2.5. B2.4 0229+23

At $z = 3.420$ (Snellen et al. 2002), this source, known as NVSS J023220+231756, shows in the VLASS image a compact structure, coincident with a bright X-ray source that in Figure 5 we indicate as region 1. We identify this region as the source nucleus, for which we estimated the broadband flux of $58^{+3}_{-3} \times 10^{-14}$ erg cm^{-2} s^{-1} (see Section 3.1). No other significant structures are visible in the broadband Chandra ACIS-S flux map.

3.2.6. B2.2 0241+30

This source, known as NVSS J024443+302117, has an FRII structure, with edge-brightened radio lobes. In Figure 5 region 1 marks the location of the faint X-ray nucleus, coincident with the radio core, for which we estimated the broadband flux of $5^{+3}_{-2} \times 10^{-15}$ erg cm^{-2} s^{-1} (see Section 3.1). On the southwest side of the nucleus there is a region of increased X-ray flux coincident with the southwestern radio lobe (region 2). This region contains 7 broadband counts, being marginally significant at the 3σ level above the emission at the same radial distance from the nucleus.

3.2.7. B2.2 0302+31

This source, also known as NVSS J030524+312928, shows evidence of significant extended X-ray emission (see Figure 4), with the western radio lobe showing an FRII edge-brightened structure, while the eastern lobe appears edge-darkened as in FRI radio sources. The global radio structure, roughly connected with the X-ray diffuse emission, can be therefore classified as a hybrid-morphology radio source (HyMoR; Gopal-Krishna & Wiita 2000). In addition, the eastern radio jet appears bent in the southeastern direction, most evidently in the LOFAR data (see Figure 1), as observed in wide-angle-tailed radio galaxies (WATs; Owen & Rudnick 1976; Leahy 1993), which usually coincide with the brightest galaxy at the center of a cluster (Missaglia et al. 2019). This source shows no identifiable nuclear emission, either in the radio or in the X-ray band. In correspondence with the western radio lobe, there is a region of increased flux (region 1 in Figure 5) that, with 29 broadband counts, significantly rises above the level of the surrounding emission at the 5σ level.

3.2.8. B2.4 0401+23

This source, known as NVSS J040452+240656, shows an edge-brightened FRII structure. Region 1 in Figure 5 marks the

Table 2
Results of Nuclear Spectral Fits with a Simple Power-law Model (plus Galactic Absorption) for Sources with Enough Counts in Their Nuclear Region

Source Name	Γ	Norm. (10^{-5} cm^{-2} s^{-1})	Pileup Frac.	c (d.o.f.)	$F_{0.3-7\ \mathrm{keV}}$ (10^{-13} erg cm^{-2} s^{-1})
B2.4 0004+21	$0.33^{+0.16}_{-0.16}$	$0.85^{+0.18}_{-0.16}$	⋯	0.88 (456)	$2.08^{+0.59}_{-0.58}$
B2.4 0145+22	$0.59^{+0.23}_{-0.47}$	$0.67^{+0.61}_{-0.33}$	⋯	0.96 (313)	$1.07^{+1.07}_{-0.57}$
B2.4 0229+23	$1.20^{+0.10}_{-0.10}$	$5.90^{+0.65}_{-0.59}$	⋯	1.04 (510)	$5.20^{+0.71}_{-0.78}$
B2.4 0401+23	$0.67^{+0.41}_{-0.42}$	$0.29^{+0.17}_{-0.11}$	⋯	1.01 (329)	$0.44^{+0.64}_{-0.25}$
B2.2 0410+26	$1.36^{+0.83}_{-0.79}$	$0.15^{+0.19}_{-0.09}$	⋯	1.01 (312)	$0.15^{+0.18}_{-0.10}$
B2.4 0412+23	$1.78^{+0.14}_{-0.14}$	$4.46^{+0.62}_{-0.55}$	⋯	1.08 (450)	$2.47^{+0.26}_{-0.18}$
B2.3 0454+35	$1.53^{+0.09}_{-0.09}$	$10.39^{+1.01}_{-0.94}$	⋯	1.06 (510)	$7.04^{+0.70}_{-0.79}$
B2.1 0536+33B	$1.36^{+0.51}_{-0.48}$	$0.33^{+0.19}_{-0.13}$	⋯	0.98 (331)	$0.26^{+0.13}_{-0.10}$
B2.1 0549+29	$2.11^{+0.39}_{-0.38}$	$1.34^{+0.55}_{-0.41}$	⋯	0.94 (343)	$0.73^{+0.20}_{-0.30}$
B2.1 0643+30	$1.75^{+0.27}_{-0.27}$	$1.29^{+0.35}_{-0.29}$	⋯	1.09 (366)	$0.81^{+0.25}_{-0.25}$
B2.1 0742+31	$2.04^{+0.07}_{-0.15}$	$55.39^{+3.06}_{-2.92}$	0.21	0.95 (675)	$27.75^{+1.34}_{-1.39}$
B2.2 1334+27	$1.84^{+0.28}_{-0.28}$	$1.55^{+0.40}_{-0.33}$	⋯	1.02 (310)	$0.83^{+0.29}_{-0.21}$
B2.2 2104+24	$1.53^{+0.11}_{-0.11}$	$4.02^{+0.42}_{-0.39}$	⋯	1.06 (470)	$2.63^{+0.37}_{-0.23}$
B2.3 2254+35	$2.73^{+1.18}_{-0.92}$	$0.40^{+0.42}_{-0.24}$	⋯	1.01 (327)	$0.31^{+0.21}_{-0.17}$
B2.2 2328+26	$0.97^{+1.07}_{-1.07}$	$0.16^{+0.18}_{-0.09}$	⋯	0.93 (310)	$0.17^{+0.10}_{-0.05}$

Note. For each source we show the power-law slope (Γ), the power-law normalization (Norm.), the pileup fraction estimated with the JDPILEUP model (Pileup Frac.), the reduced Cash statistics and degrees of freedom, and the intrinsic 0.3–7 keV flux obtained from spectral fitting ($F_{0.3-7\ \mathrm{keV}}$).

X-ray nucleus with a flux of $4^{+1}_{-1} \times 10^{-14}$ erg cm^{-2} s^{-1} (see Section 3.1). Along the radio axis there are two regions of increased X-ray flux (regions 2 and 3 in Figure 5); however only region 3 with its 6 broadband counts is marginally significant at the 3σ level above the emission at the same radial distance from the nucleus.

3.2.9. B2.2 0410+26

This source, also known as NVSS J041323+264916, shows a rather compact radio structure in both the LOFAR and the VLASS radio map, where only the core is detected. Region 1 marks the faint X-ray nucleus with an $11^{+4}_{-3} \times 10^{-15}$ erg cm^{-2} s^{-1} flux (see Section 3.1) in correspondence with the radio core. No other significant structures are visible in the broadband Chandra ACIS-S flux map.

3.2.10. B2.4 0412+23

This source, also known as NVSS J041512+234751, shows a radio structure elongated in the north–south direction, as shown in the LOFAR and GMRT data. The VLASS image shows the radio core and the two compact radio lobes. Apart from the bright X-ray nucleus coincident with the radio core (labeled region 1 in Figure 5) with a broadband flux of $27^{+2}_{-2} \times 10^{-14}$ erg cm^{-2} s^{-1} (see Section 3.1), B2.4 0412+23 has evidence of extended X-ray emission (see Figure 4), with several regions of extended flux along the radio axis (region 2 in Figure 5), in correspondence with the radio lobes (regions 3 and 4 in Figure 5) and with the western side of the nucleus (region 5 in Figure 5). These regions however have a low $\lesssim 2\sigma$ significance with respect to the surrounding emission, with the exception of region 5, which with 16 broadband counts reaches a significance of almost 6σ.

3.2.11. B2.3 0454+35

This source shows an elongated radio structure in the north–south direction. In particular the GMRT and VLASS data indicate a bright hot spot in the north and a narrow jet in the southern direction—possibly a one-sided relativistic jet—that originates from a bright compact X-ray source (region 1 in Figure 5) with a broadband flux of $80^{+3}_{-3} \times 10^{-14}$ erg cm^{-2} s^{-1} (see Section 3.1), which we identify as the X-ray nucleus. No other radio structure (including the northern hot spot) shows significant X-ray emission.

3.2.12. B2.1 0455+32B

This source, also known as NVSS J045906+323613, shows a rather compact radio structure in LOFAR and GMRT images. Its VLASS data instead reveal two compact radio lobes along the east–west direction. Between these two lobes there is a faint X-ray source (region 1 in Figure 5) with a broadband flux of $8^{+4}_{-3} \times 10^{-15}$ erg cm^{-2} s^{-1} (see Section 3.1), possibly the nucleus of the source. The two radio lobes do not show any significant X-ray emission.

3.2.13. B2.1 0455+32C

The LOFAR and VLASS images of this source, also known as NVSS J045913+322607, show two radio lobes along the east–west direction, with a hint of an edge-brightened FRII structure. Between the radio lobes there is a faint X-ray source (region 1 in Figure 5) with a broadband flux of $7^{+4}_{-3} \times 10^{-15}$ erg cm^{-2} s^{-1} (see Section 3.1), which we identify as the source nucleus. No other radio structure shows significant X-ray emission.

3.2.14. B2.3 0516+40

This source (also known as NVSS J051946+401507) shows a compact radio structure. The nuclear region (marked 1 in Figure 5) has a faint broadband X-ray flux of $4^{+4}_{-3} \times 10^{-15}$ erg cm^{-2} s^{-1} (see Section 3.1). There are two compact regions of enhanced X-ray emission southwest of the nucleus (regions 2 and 3 in Figure 5), which, compared to the level of the diffuse emission at the same radial distance from the nucleus, have a significance of $>3\sigma$ and $>4\sigma$, respectively. However, they appear disconnected from the radio structure.

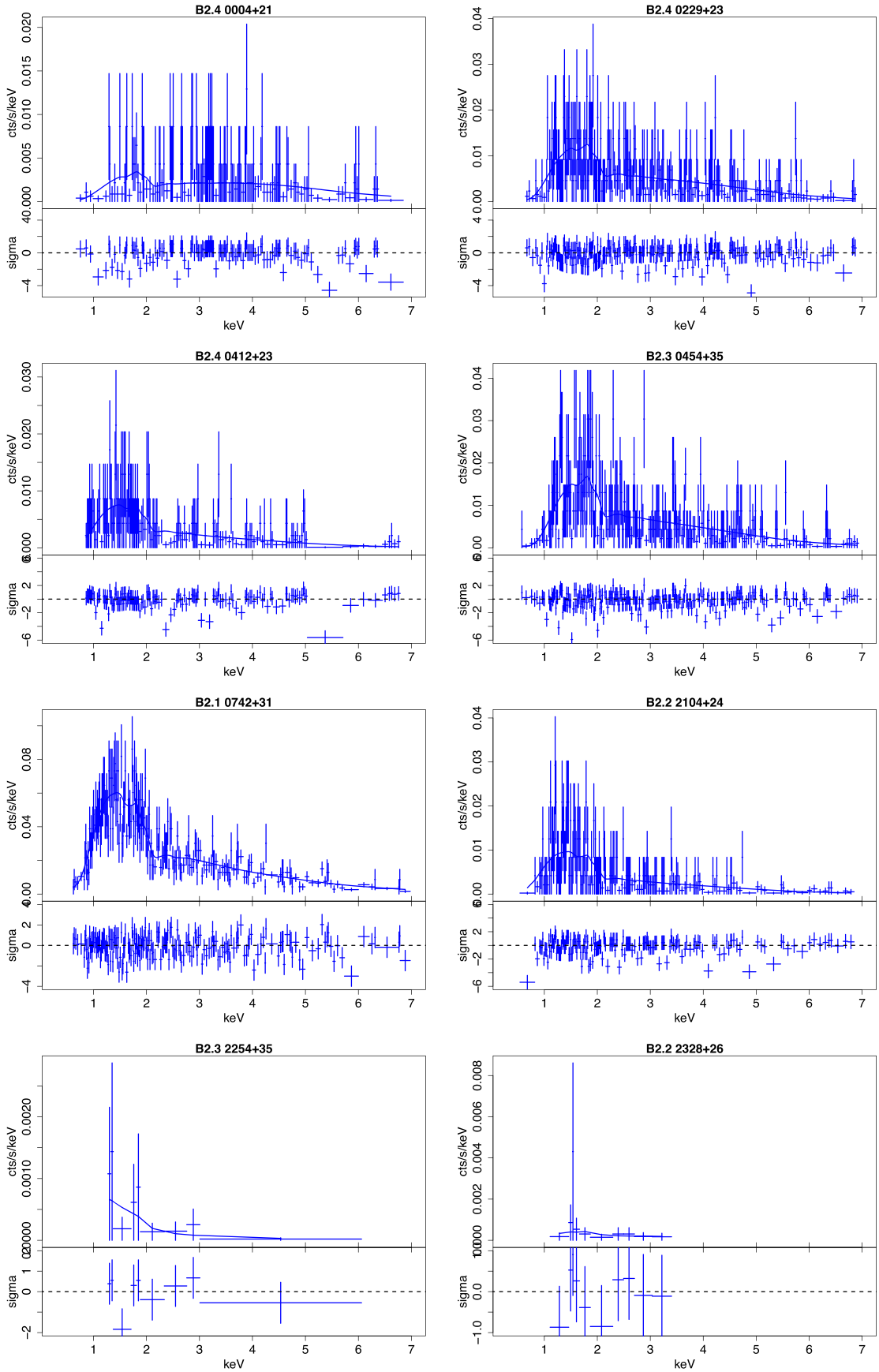

Figure 6. Nuclear spectral fits presented in Table 2 with a power law plus Galactic absorption model. For each source, in the upper part of the panel, we show the extracted spectrum with blue crosses and the best-fit model with a blue line, while in the lower part of the panel we show the residuals.

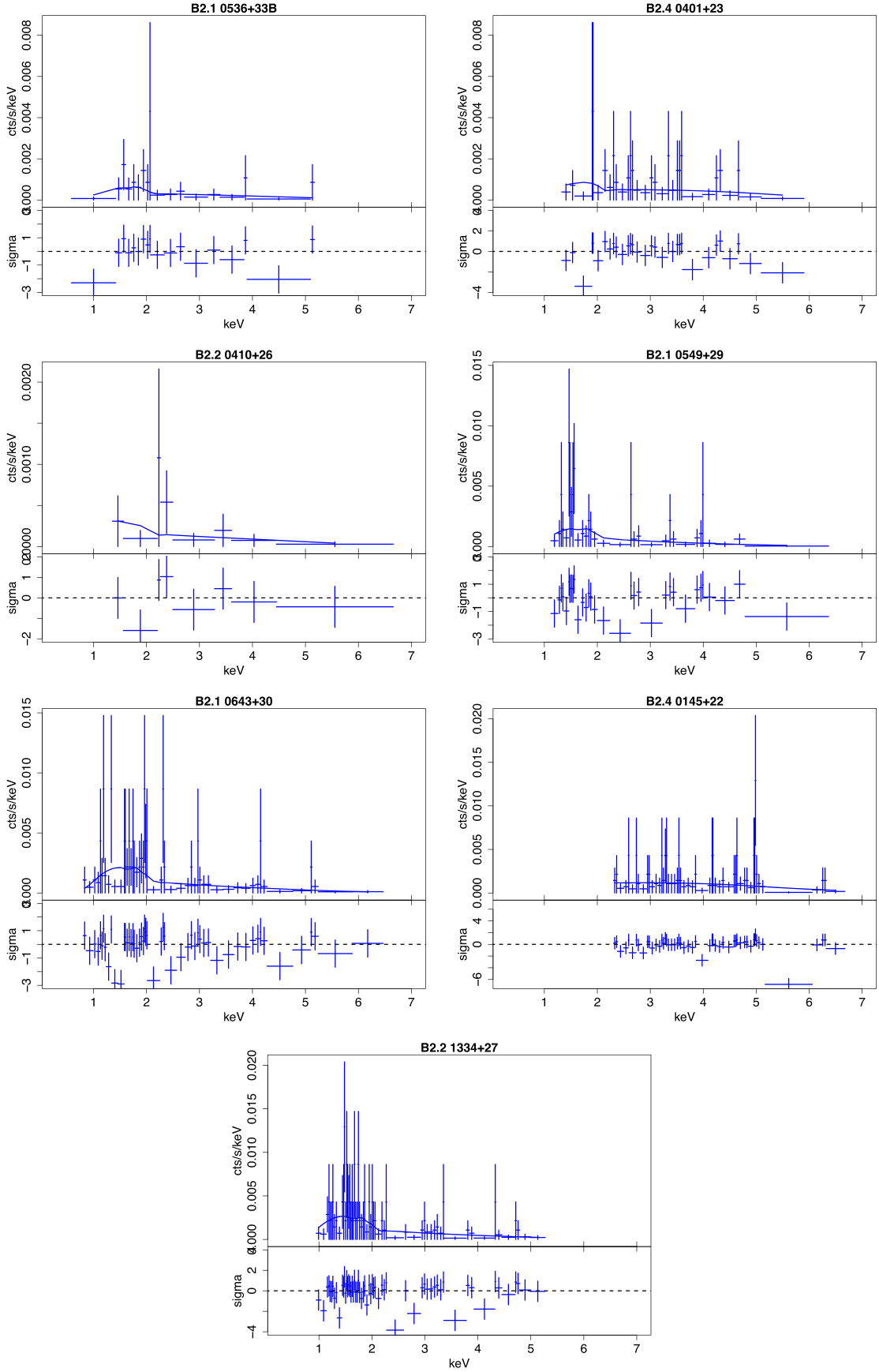

Figure 6. (Continued.)

Table 3
Same as Table 2, but for a Fitting Model that Includes an Additional Absorbing Component, and with a Power-law Slope Fixed to 1.8

Source Name	$N_{H,int}$ (10^{22} cm^{-2})	Norm. (10^{-5} cm^{-2} s^{-1})	Pileup Frac.	c (d.o.f.)	$F_{0.3-7\ keV}$ (10^{-13} erg cm^{-2} s^{-1})
B2.4 0004+21	$2.14^{+0.33}_{-0.31}$	$7.95^{+0.91}_{-0.83}$	⋯	0.87 (456)	$4.49^{+0.39}_{-0.58}$
B2.4 0145+22	$5.07^{+1.88}_{-2.04}$	$5.70^{+1.31}_{-1.26}$	⋯	0.96 (313)	$3.15^{+0.13}_{-0.10}$
B2.4 0229+23	$24.02^{+4.96}_{-4.80}$	$13.84^{+1.12}_{-1.05}$	⋯	1.06 (510)	$7.65^{+0.60}_{-0.60}$
B2.4 0401+23	$2.10^{+0.78}_{-0.70}$	$1.70^{+0.46}_{-0.38}$	⋯	1.00 (329)	$0.95^{+0.20}_{-0.27}$
B2.2 0410+26	<2.29	$0.31^{+0.20}_{-0.13}$	⋯	1.01 (312)	$0.17^{+0.08}_{-0.06}$
B2.4 0412+23	<0.05	$4.53^{+0.32}_{-0.30}$	⋯	1.08 (450)	$2.52^{+0.12}_{-0.10}$
B2.3 0454+35	$0.21^{+0.09}_{-0.08}$	$14.71^{+0.91}_{-0.86}$	⋯	1.07 (510)	$8.12^{+0.50}_{-0.42}$
B2.1 0536+33B	$0.63^{+0.55}_{-0.43}$	$0.66^{+0.54}_{-0.18}$	⋯	0.98 (331)	$0.37^{+0.11}_{-0.09}$
B2.1 0549+29	<0.16	$1.03^{+0.18}_{-0.16}$	⋯	0.94 (343)	$0.59^{+0.09}_{-0.09}$
B2.1 0643+30	<0.23	$1.37^{+0.26}_{-0.19}$	⋯	1.09 (366)	$0.79^{+0.12}_{-0.20}$
B2.1 0742+31	<0.02	$53.83^{+3.12}_{-2.84}$	0.14	0.95 (675)	$29.76^{+1.13}_{-1.35}$
B2.2 1334+27	<13.99	$1.62^{+0.36}_{-0.27}$	⋯	1.02 (310)	$0.88^{+0.12}_{-0.13}$
B2.2 2104+24	$0.21^{+0.07}_{-0.07}$	$5.80^{+0.47}_{-0.44}$	⋯	1.04 (470)	$3.17^{+0.20}_{-0.24}$
B2.3 2254+35	<0.49	$0.20^{+0.08}_{-0.06}$	⋯	1.02 (327)	$0.11^{+0.03}_{-0.03}$
B2.2 2328+26	<1.56	$0.41^{+0.30}_{-0.18}$	⋯	0.93 (310)	$0.22^{+0.04}_{-0.03}$

Note. For each source we show the additional absorbing column density ($N_{H,int}$), the power-law normalization (Norm.), the pileup fraction estimated with the JDPILEUP model (Pileup Frac.), the reduced Cash statistics and degrees of freedom, and the intrinsic 0.3–7 keV flux obtained from spectral fitting ($F_{0.3-7\ keV}$).

3.2.15. B2.1 0536+33B

This source, known as NVSS J054003+334200, shows an edge-brightened FRII structure in its VLASS image elongated in the east–west direction. Region 1 in Figure 5 marks the X-ray nucleus with a $29^{+7}_{-6} \times 10^{-15}$ erg cm^{-2} s^{-1} flux (see Section 3.1). No other significant structures are visible in the broadband Chandra ACIS-S flux map.

3.2.16. B2.1 0549+29

VLASS data show for B2.1 0549+29, also known as NVSS J055255+293203, a rather compact radio structure, with a core and two lobes along the east–west direction. In Figure 5 region 1 marks the X-ray nucleus with a $7^{+1}_{-1} \times 10^{-14}$ erg cm^{-2} s^{-1} flux (see Section 3.1). Also in this case, no other significant structures are visible in the broadband Chandra ACIS-S flux map.

3.2.17. B2.1 0643+30

The radio structure of this source (also known as NVSS J064615+304123) as imaged by VLASS is compact, showing only the core emission coincident with the X-ray nucleus emitting an $8^{+1}_{-1} \times 10^{-14}$ erg cm^{-2} s^{-1} broadband flux (see Section 3.1), marked in Figure 5 as region 1. Again, the broadband Chandra ACIS-S flux map shows no other significant structures.

3.2.18. B2.1 0742+31

This source (also known as NVSS J074542+314252) at a redshift of 0.461 (Kerr & Lynden-Bell 1986) features an FRII edge-brightened radio structure as shown in LOFAR and VLASS data (see Figure 1). This source has the brightest X-ray nucleus of the present sample (marked region 1 in Figure 5), with an estimated flux of $219^{+5}_{-5} \times 10^{-14}$ erg cm^{-2} s^{-1} (see Section 3.1), and is therefore affected by significant pileup (see Section 3.3). In addition, B2.1 0742+31 shows significant diffuse X-ray emission (see Figure 4), both along the radio axis and across it, as shown in Figure 5. In particular, there are two regions of increased X-ray flux, one north of the nucleus (region 2) and another in correspondence with the southeastern radio lobe (region 3). Region 2, located north of the nucleus and connected with the emission surrounding the latter, contains 17 broadband counts, while region 3 contains 30 broadband counts. Both regions are significant at the 4σ level with respect to the surrounding emission.

3.2.19. B2.2 0755+24

This source (also known as NVSS J075802+242219), at a redshift of 0.502 (Garon et al. 2019), has a compact radio structure, where only the radio lobes are visible in VLASS data (see Figure 1). In Figure 5 we mark as region 1 the location that we identify as the faint X-ray nucleus, with an estimated broadband flux of $8^{+4}_{-3} \times 10^{-15}$ erg cm^{-2} s^{-1} (see Section 3.1). No other significant structures are visible in the broadband Chandra ACIS-S flux map.

3.2.20. B2.3 0848+34

This source (also known as J085108+341925), at a redshift of 0.697 (Alam et al. 2015), shows a rather compact radio structure as imaged by LOFAR, with a slight extension toward the south. The VLASS data reveal a slightly elongated structure, with two small lobes along the east–west direction. Between the lobes we see a compact region of increased X-ray flux (marked 1 in Figure 5) with a broadband X-ray flux of $9^{+4}_{-3} \times 10^{-15}$ erg cm^{-2} s^{-1} (see Section 3.1), which we identify as the source nucleus. Besides this nuclear region, there are no significant structures in the broadband Chandra ACIS-S flux map.

3.2.21. B2.4 0939+22A

This source (also known as NVSS J094158+214743), with a redshift of 0.572 (Saripalli & Roberts 2018), has an FRII radio structure, as imaged with VLASS, with the radio axis aligned

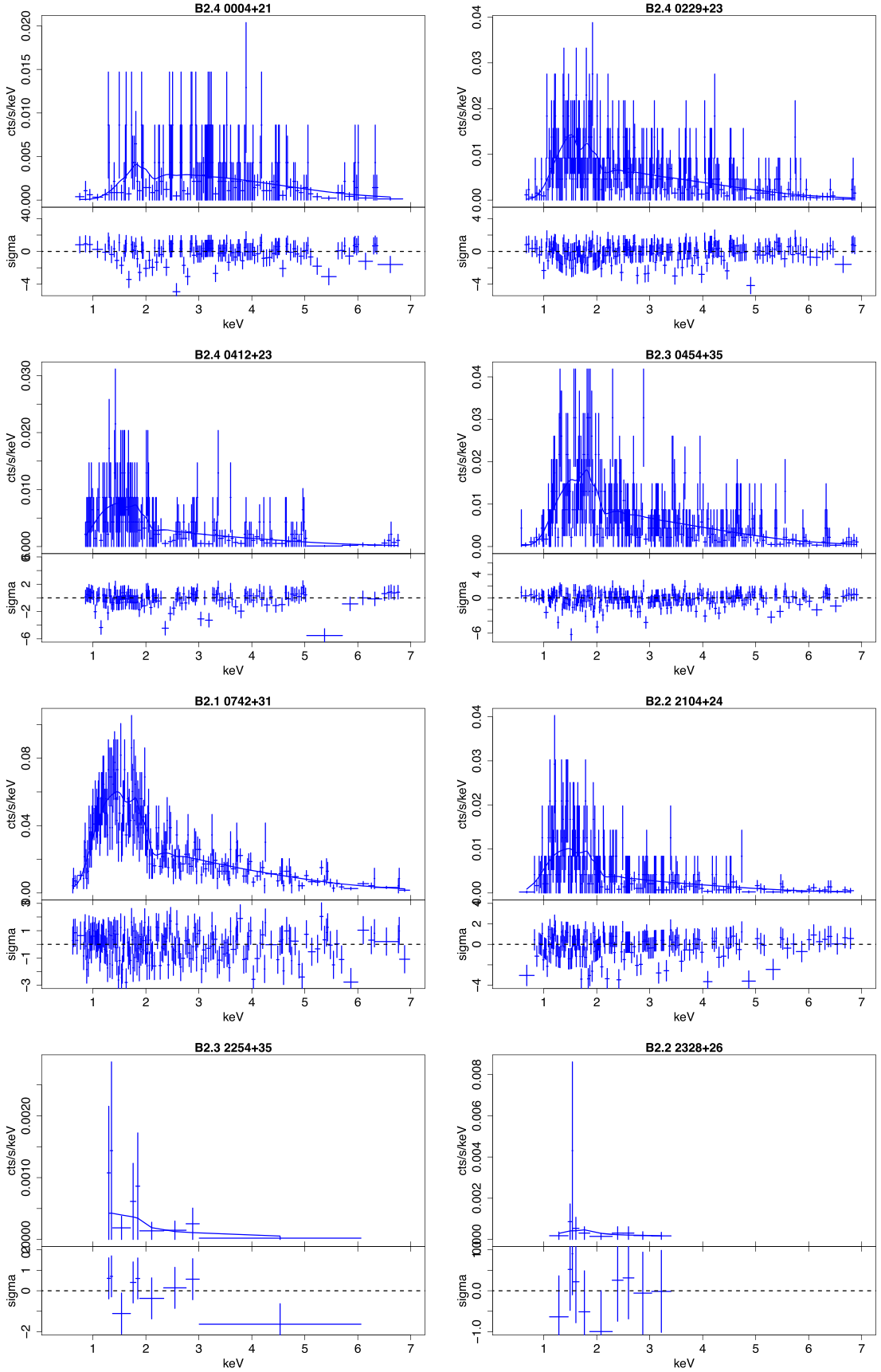

Figure 7. Nuclear spectral fits presented in Table 3 with a power-law model with slope fixed to 1.8 plus Galactic absorption, and an additional absorption component. For each source, in the upper part of the panel we show the extracted spectrum with blue crosses and the best-fit model with a blue line, while in the lower part of the panel we show the residuals.

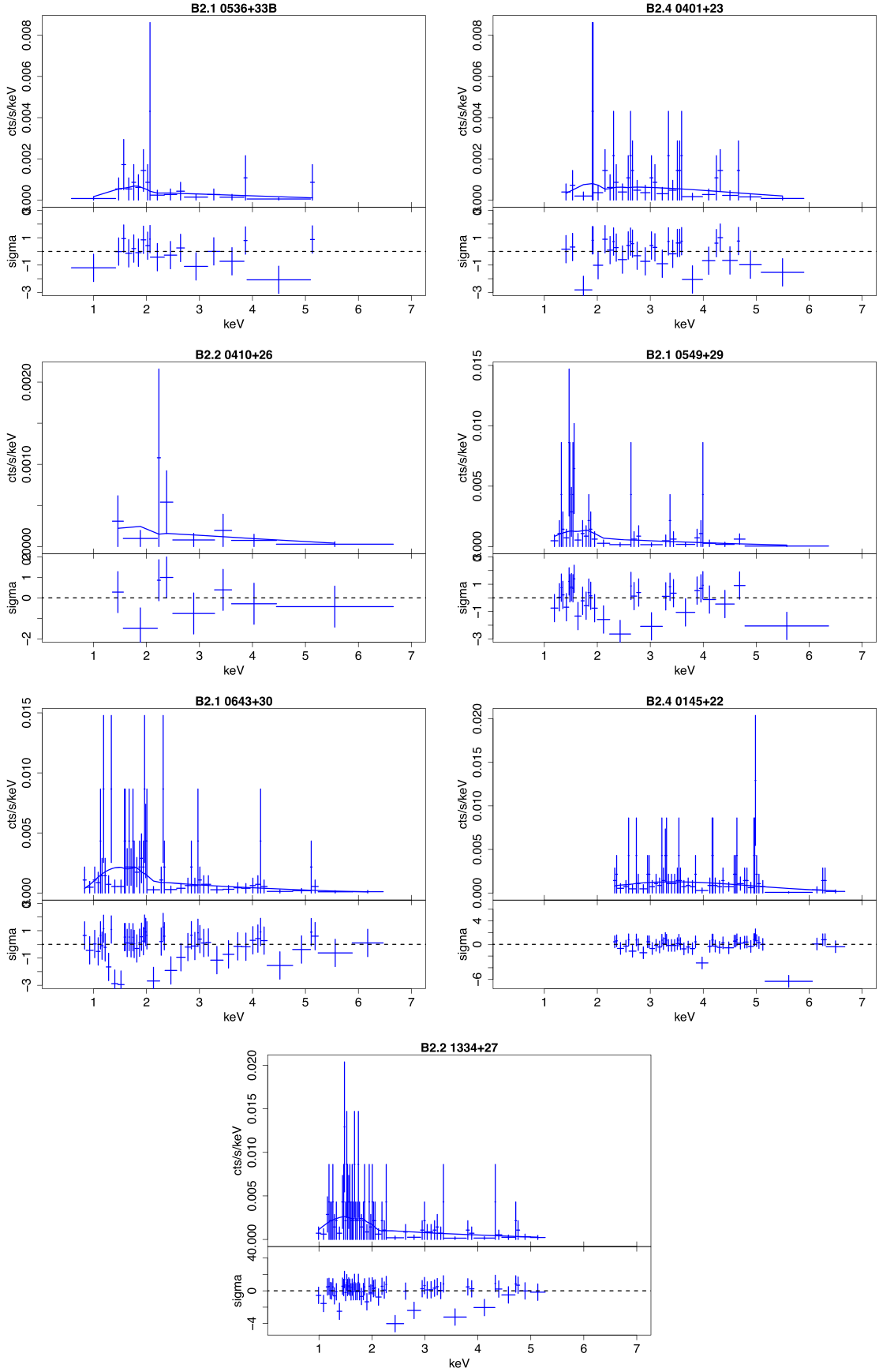

Figure 7. (Continued.)

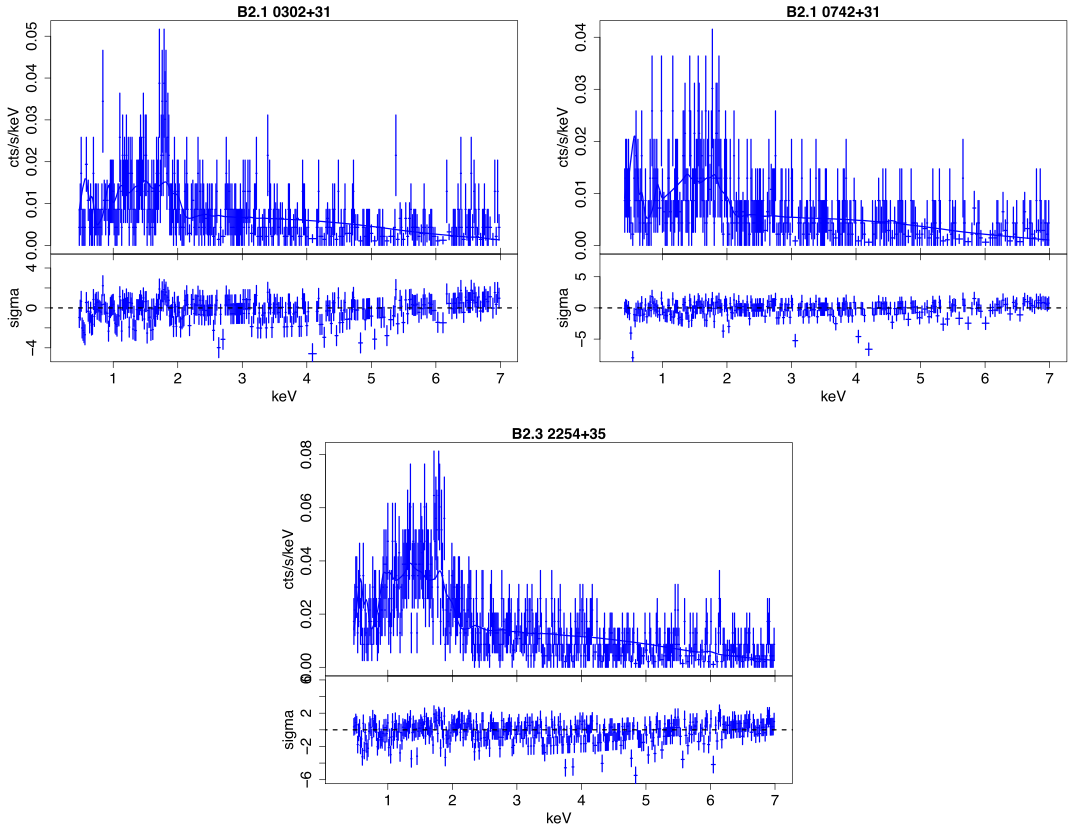

Figure 8. Spectral fits of the extended X-ray emission presented in Table 4 with a model including a thermal plasma plus Galactic absorption. For each source, in the upper part of the panel we show the extracted spectrum with blue crosses and the best-fit model with a blue line, while in the lower part of the panel we show the residuals.

along the northeast–southwest direction. The southwestern radio lobe is bent in the northwestern direction. The radio image does not show a clear core, but there is a faint pointlike region between the two radio lobes (marked as region 1 in Figure 5) that we identify as the X-ray nucleus, with a broadband flux of $9^{+4}_{-3} \times 10^{-15}$ erg cm^{-2} s^{-1} (see Section 3.1). In addition, there is a region of increased X-ray flux (region 2 in Figure 5) coincident with the northeastern radio lobe. This region contains 25 broadband counts, and it is therefore highly significant with respect to the emission at the same radial distance from the nucleus at the 7σ level.

3.2.22. B2.4 1112+23

The VLASS data of this source, also known as NVSS J111505+232503, only show the radio core, coincident with a region (marked as region 1 in Figure 5) of faint X-ray flux $6^{+4}_{-3} \times 10^{-15}$ erg cm^{-2} s^{-1} (see Section 3.1) that we identify as the source nucleus. Besides the nucleus, there are no significant structures in the broadband Chandra ACIS-S flux map.

3.2.23. B2.3 1234+37

This source, also known as NVSS J123649+365518, features two radio lobes along the northeast–southwest direction, as imaged by LOFAR and VLASS. Between the radio lobes there is a faint X-ray source (region 1 in Figure 5) with a broadband flux of $13^{+5}_{-4} \times 10^{-14}$ erg cm^{-2} s^{-1} (see Section 3.1), which we identify as the source nucleus. No other radio structure shows significant X-ray emission.

3.2.24. B2.2 1334+27

At a redshift $z = 3.228$ (Alam et al. 2015), this source, also known as NVSS J133641+270401, shows a faint extended radio structure in its LOFAR image. However, the VLASS data only reveal two compact radio lobes along the northwest–southeast direction. Between the radio lobes there is an X-ray source (region 1 in Figure 5) with a broadband flux of $9^{+1}_{-1} \times 10^{-14}$ erg cm^{-2} s^{-1} (see Section 3.1), possibly the X-ray source nucleus. No other radio structure shows significant X-ray emission.

3.2.25. B2.2 1338+27

This source, also known as NVSS J134029+272326, shows two radio hot spots along the northwest–southeast direction, as imaged by LOFAR, GMRT, and VLASS. Between the radio lobes there is a faint X-ray source (region 1 in Figure 5) with a broadband flux of $<9 \times 10^{-15}$ erg cm^{-2} s^{-1} (see Section 3.1), possibly the X-ray source nucleus. We detected no significant X-ray emission in correspondence with the radio lobes.

3.2.26. B2.2 1439+25

The VLASS data of this source, also known as NVSS J144204+250335, show an FRII radio structure extending along the north–south direction without revealing the radio core. No significant X-ray structure is revealed in the broadband Chandra ACIS-S flux map.

Table 4
Results of Spectral Fits of the Diffuse X-Ray Emission with a Thermal Plasma Model plus Galactic Absorption

Source Name	kT (keV)	Norm. (10^{-5} cm^{-5})	c (d.o.f.)	$F_{0.3-7\ \mathrm{keV}}$ (10^{-13} erg cm^{-2} s^{-1})
B2.1 0302+31	$2.45^{+0.97}_{-0.47}$	$21.78^{+2.58}_{-2.62}$	1.02 (640)	$2.53^{+0.49}_{-0.55}$
B2.1 0742+31	$1.93^{+0.56}_{-0.34}$	$40.55^{+7.82}_{-7.33}$	0.96 (607)	$1.81^{+0.23}_{-0.15}$
B2.3 2254+35	$2.47^{+0.39}_{-0.32}$	$58.38^{+4.26}_{-4.19}$	1.04 (712)	$5.34^{+0.36}_{-0.38}$

Note. For each source we show the thermal plasma temperature (kT), the thermal plasma normalization (Norm.), the reduced Cash statistics and degrees of freedom, and the intrinsic 0.3–7 keV flux obtained from spectral fitting ($F_{0.3-7\ \mathrm{keV}}$).

Table 5
Results of Spectral Fits of the Diffuse X-Ray Emission with a Thermal Plasma Model (plus Galactic Absorption), excluding the Regions Spatially Associated with Extended Radio Structures

Source Name	kT (keV)	Norm. (10^{-5} cm^{-5})	c (d.o.f.)	$F_{0.3-7\ \mathrm{keV}}$ (10^{-13} erg cm^{-2} s^{-1})
B2.1 0302+31	$2.46^{+1.30}_{-0.54}$	$12.81^{+1.98}_{-2.03}$	0.94 (587)	$1.45^{+0.26}_{-0.27}$
B2.1 0742+31	$1.93^{+5.58}_{-0.67}$	$10.24^{+5.14}_{-6.10}$	0.99 (528)	$0.48^{+0.12}_{-0.15}$
B2.3 2254+35	$2.45^{+0.54}_{-0.39}$	$32.21^{+3.09}_{-2.99}$	1.02 (648)	$2.91^{+0.20}_{-0.19}$

Note. For each source we show the thermal plasma temperature (kT), the thermal plasma normalization (Norm.), the reduced Cash statistics and degrees of freedom, and the intrinsic 0.3–7 keV flux obtained from spectral fitting ($F_{0.3-7\ \mathrm{keV}}$).

3.2.27. B2.4 1512+23

This source (also known as NVSS J151414+232711), at a redshift of 0.088 (Ahn et al. 2012), shows an FRII radio structure extending along the north–south direction, as imaged by VLASS. In particular, the southern lobe appears connected to the central region with a jet-shaped structure, originating from a bright X-ray compact region (marked 1 in Figure 5) with broadband X-ray flux of $16^{+5}_{-5} \times 10^{-14}$ erg cm^{-2} s^{-1} (see Section 3.1), which we identify as the source nucleus. There are regions of enhanced X-ray emission in correspondence with the northern lobe (region 2 in Figure 5) and with the southern hot spot (region 3 in Figure 5). Region 3 has a low $<2\sigma$ significance, while region 2 is significant at a 4σ level with respect to the level of the diffuse emission at the same radial distance from the nucleus.

3.2.28. B2.4 2054+22B

This source, known as NVSS J205658+222954, shows an FRII radio structure in VLASS data, with lobes extending across the east–west direction. A faint region of enhanced X-ray emission (indicated as region 1 in Figure 5) features a broadband flux of $6^{+4}_{-3} \times 10^{-15}$ erg cm^{-2} s^{-1} (see Section 3.1), which we identify as the source nucleus. North of the nucleus there is another compact region of increased X-ray flux (region 2 in Figure 5) that is significant at the 3σ level compared to the level of the diffuse emission at the same radial distance from the nucleus. This region, however, does not appear to be clearly connected with the radio structure.

3.2.29. B2.2 2104+24

This source, known as NVSS J210621+243324, shows an FRII VLASS radio structure, with a bright X-ray nucleus (region 1 in Figure 5) emitting a broadband flux of $30^{+2}_{-2} \times 10^{-14}$ erg cm^{-2} s^{-1} (see Section 3.1). Besides the nucleus, there are no significant X-ray structures in the broadband Chandra ACIS-S flux map.

3.2.30. B2.2 2133+27

The radio structure of this source (known as NVSS J213516 +271626), as imaged by VLASS, does not have a clear shape, with the radio axis lying along the northwest–southeast direction, and with no clear radio core detection. There seems to be a region of increased X-ray flux in correspondence with the northwestern radio lobe (indicated as region 1 in Figure 5), but its significance with respect to the surrounding emission is only at the 2σ level.

3.2.31. B2.3 2254+35

This source (also known as NVSS J225645+354127), at a redshift of 0.114 (Bilicki et al. 2014), has a complex radio and X-ray morphology. The VLASS data reveal the location of the radio core and an edge-darkened FRI structure, with a jet extending toward the northern direction, and another extending toward the eastern direction. The latter jet, in particular, appears bent in the southeastern direction at larger radii, as even more evident in the large-scale LOFAR data (see Figure 1), revealing a WAT morphology. Region 1 in Figure 5 is coincident with the radio core, and emits a broadband X-ray flux of $10^{+4}_{-3} \times 10^{-15}$ erg cm^{-2} s^{-1} (see Section 3.1). The X-ray emission is clearly extended (see Figure 4) and shows a complex morphology with two regions of decreased flux (marked 2 and 3 in Figure 5) that look like X-ray cavities. Region 2, however, is less luminous than the emission at the same radial distance from the nucleus, only at the 2σ level, while for region 3 this significance increases to the $\sim 4\sigma$ level.

3.2.32. B2.2 2328+26

The radio structure of this source (known as NVSS J233032 +270614) as mapped by VLASS appears slightly elongated in the northeast–southwest direction. The region marked 1 in Figure 5 indicates the pointlike source that we identify as the

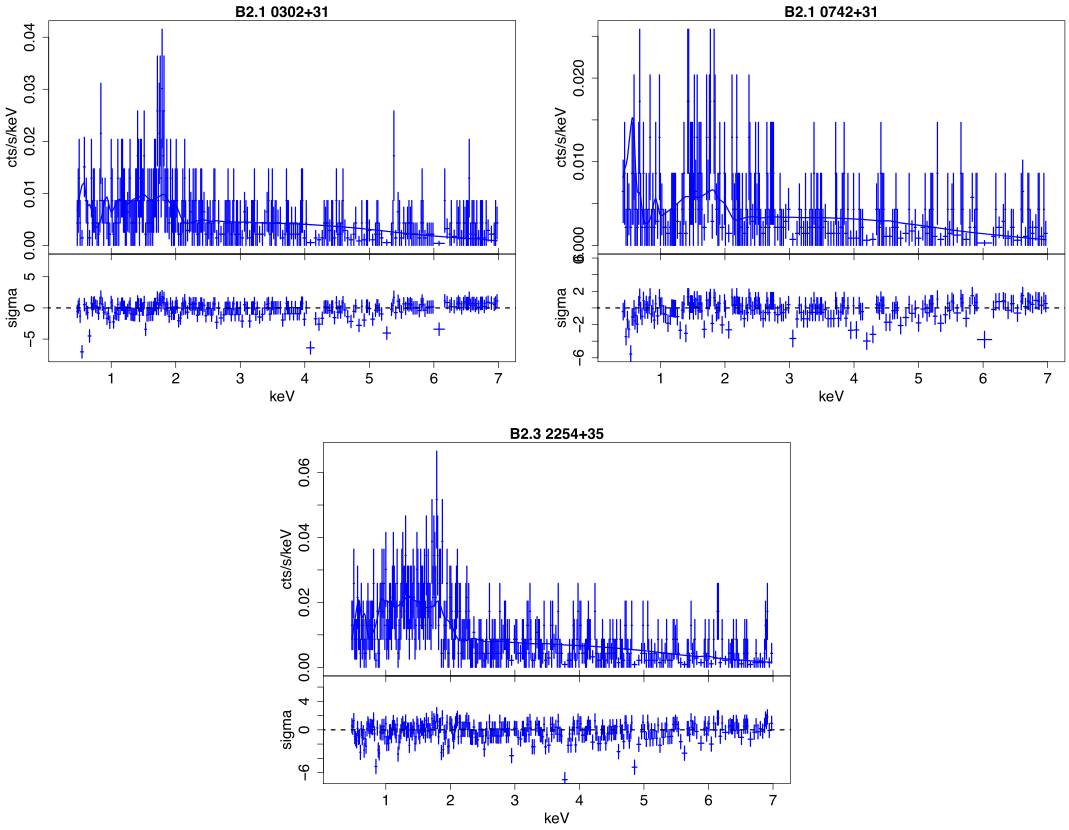

Figure 9. Spectral fits of the extended X-ray emission (excluding the regions connected with extended radio structures) presented in Table 5 with a model including a thermal plasma plus Galactic absorption. For each source, in the upper part of the panel we show the extracted spectrum with blue crosses and the best-fit model with a blue line, while in the lower part of the panel we show the residuals.

X-ray nucleus, with a broadband flux of $12^{+0.4}_{-0.4} \times 10^{-15}$ erg cm^{-2} s^{-1} (see Section 3.1). This is the only significant X-ray feature revealed in the broadband Chandra ACIS-S flux map.

3.2.33. B2.3 2334+39

The VLASS data of this source, also known as NVSS J233655+400546, only reveal the location of the radio core and that of the lobes, aligned along the northwest–southeast direction. The LOFAR data (see Figure 1), on the other hand, indicate an FRI edge-darkened radio morphology, with the southeastern lobe bending toward the northeastern direction, and the northwestern lobe bending toward the southeastern direction. The region marked 1 in Figure 5 indicates the faint pointlike source that we identify as the X-ray nucleus, with a broadband flux $<5 \times 10^{-15}$ erg cm^{-2} s^{-1} (see Section 3.1). There are no other significant X-ray features in the broadband Chandra ACIS-S flux map.

3.3. Spectral Analysis

To characterize in more detail the sources in the present sample, we performed a spectral analysis of their nuclear emission. We extracted nuclear spectra in a 2″ circular region centered at the coordinates of the radio or X-ray core, while background spectra were extracted in source-free regions as close as possible to the nuclear extraction region to avoid vignetting effects at the CCD edge, but far enough to exclude contamination from eventual diffuse emission. We produced auxiliary response files and spectral response matrices for both the nuclear and background spectra, applying for the former point-source aperture corrections (as appropriate for pointlike sources). Spectral fitting was performed in the 0.3–7 keV energy range with the SHERPA application (Freeman et al. 2001).

Due to the low counts, we performed the spectral fits by modeling the background spectra using the prescription given by Markevitch et al. (2003), that is, a model comprising a thermal plasma component (MEKAL; Kaastra 1992) with solar abundances and a power law. We modeled the nuclear spectra with a power-law (POWERLAW) model, including photoelectric absorption (XSTBABS) by the Galactic column density along the line of sight (HI4PI Collaboration et al. 2016). In addition, for the source B2.1 0742+31 we included the JDPILEUP model (Davis 2001) to account for the ACIS-S detector pileup. The spectra were binned to obtain a minimum of 1 count per bin, making use of the Cash statistic (Paggi et al. 2021).

Following this procedure we were able to extract and fit nuclear spectra for 15 sources. The results of these fits are presented in Table 2 and in Figure 6. Uncertainties correspond to the 1σ confidence level for one interesting parameter. We note that in many spectra we detect very few counts below 1 keV, as a result of the degrading Chandra effective area at low energies. We see that the intrinsic fluxes estimated from these spectral fits are compatible with those evaluated with SRCFLUX (see Section 3.1), with the exception of that for B2.1 0742+31—for which the JDPILEUP model estimates a pileup fraction of ∼20%, compatible with the value obtained from the

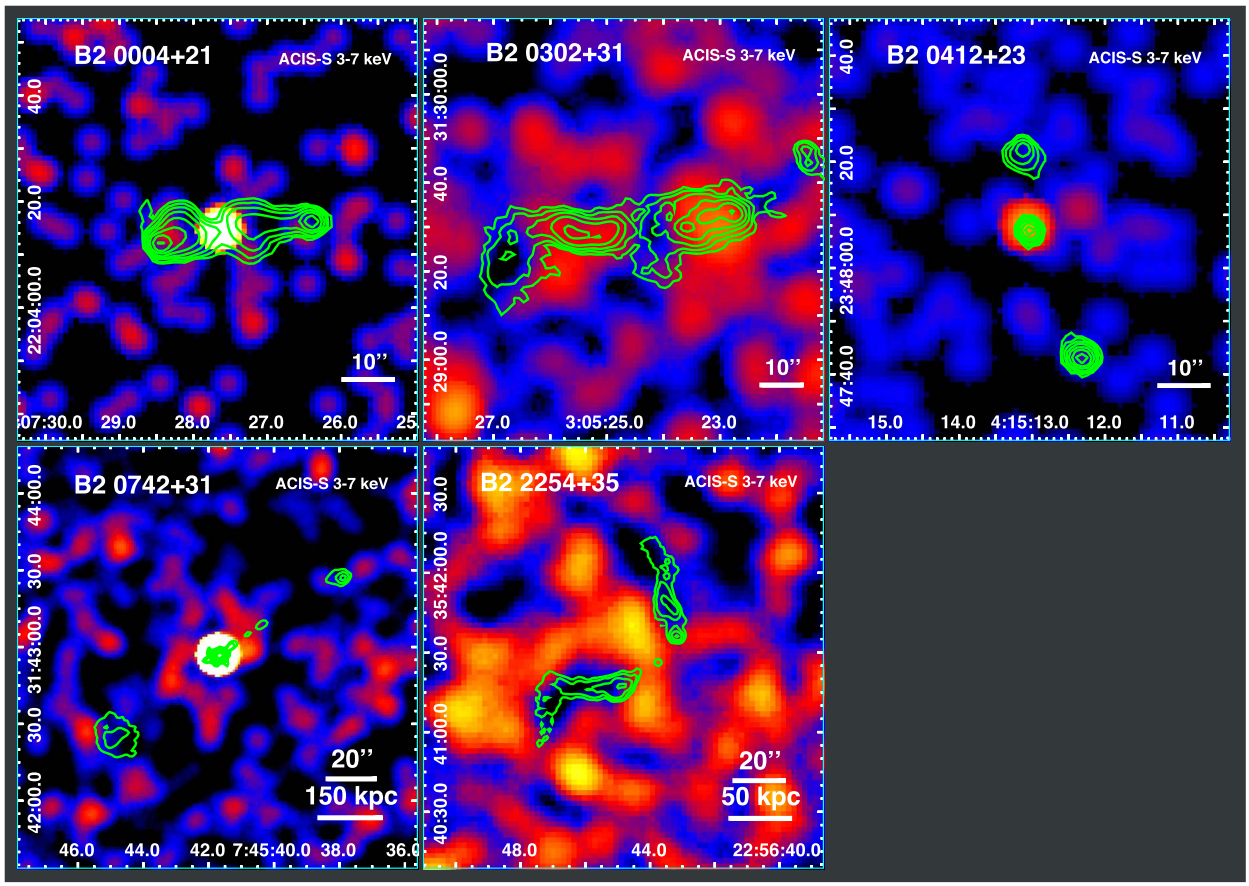

Figure 10. Hard-band 3–7 keV Chandra ACIS-S flux maps for sources in the present sample that show evidence of extended X-ray emission (see Section 3.1). The VLASS 3 GHz contours overlaid in green are the same ones from Figure 1.

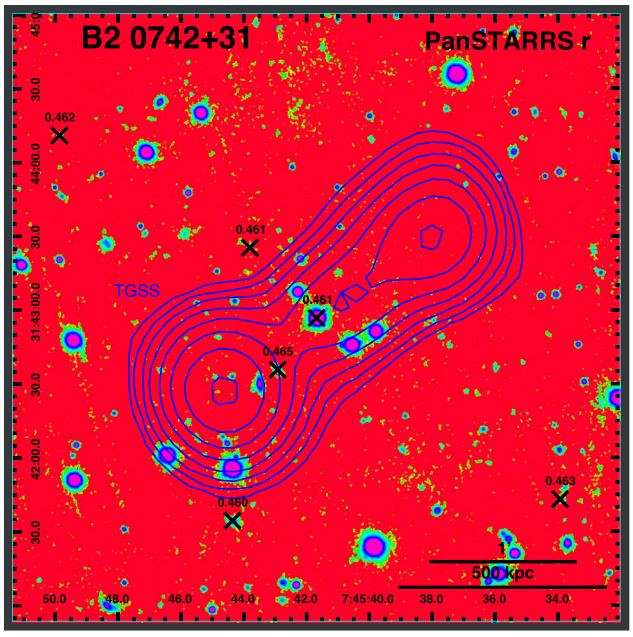

Figure 11. Pan-STARRS (Chambers et al. 2016) r_{P1} filter image of B2.1 0742 +31, with overlaid in blue the 150 MHz TGSS contours from Figure 1. Black crosses indicate, in addition to the galaxy hosting the radio source, field sources with redshift measurements close to that of B2.1 0742+31 (0.461). The redshift value is indicated next to each cross.

pileup map. In addition, we notice that, while in a number of sources we find slopes $\Gamma \sim 1.5$–2.0—compatible with what is observed in similar sources (Hardcastle et al. 2006, 2009; Mingo et al. 2014)—in others the spectral fit yields particularly flat slopes, indicating the possible presence of significant intrinsic absorption.

To investigate the presence of intrinsic absorption, we repeated the spectral fitting of the nuclear spectra freezing the power-law slope to 1.8 and considering an additional absorption component (XSZTBABS) at the source redshift or, if this measurement was not available, at redshift zero. The results of these fits are presented in Table 3 and in Figure 7. For most of the sources we are only able to put upper limits on the intrinsic absorption column, or find values compatible with the Galactic ones. For the sources B2.4 0004+21, B2.4 0145+212, and B2.4 0401+23, we find intrinsic absorbing columns $\sim 10^{22}\,\mathrm{cm}^{-2}$, while for the source B2.4 0229+23 we find an additional absorbing column of $\sim 10^{23}\,\mathrm{cm}^{-2}$, all significantly larger than the Galactic values.

As discussed in Section 3.1, we have five sources that show evidence of significant extended emission in the soft 0.3–3 keV band (see Figure 4). We extracted source spectra in large elliptical regions that encompass the whole extended emission visible in the flux maps (see Figure 1), excluding detected point sources as well as the $2''$ nuclear regions. Background spectra were extracted in the same source-free regions used for the

nuclear spectral fitting. In this case, we produced spectral response matrices weighted by the count distribution within the aperture (as appropriate for extended sources).

We used the same procedure adopted for the nuclear spectral fitting, that is, modeling the background spectra and using the Cash statistics, with the spectra binned to obtain a minimum of 1 count per bin. The sources B2.4 0004+21 and B2.4 0412+23 did not yield enough counts to allow a reasonable fit, and were therefore excluded from the following analysis. To fit the spectra of the extended emission we used a model comprising the Galactic absorption and a thermal plasma (XSAPEC[26]) with 0.25 solar abundance (as expected from typical ICM emission). The redshift of the thermal plasma was set at the value of the source redshift or, if this measurement was not available, at redshift zero.

The results of these fits are presented in Table 4 and in Figure 8. Again, uncertainties correspond to the 1σ confidence level for one interesting parameter. We obtain reasonable best-fit temperatures between 1.9 and 2.5 keV. The diffuse emission surrounding these sources, however, can be a combination of thermal emission from hot gas of the ICM and IC/CMB. To minimize contamination from such nonthermal emission, we repeated the spectral extraction excluding the regions of extended radio emission shown in Figure 1. The results of these fits are presented in Table 5 and in Figure 9. The temperature values obtained in this way are similar to those obtained previously (although with larger uncertainties), suggesting that in these sources the contribution from nonthermal IC/CMB emission could be subdominant with respect to the thermal radiation arising from the ICM. Since the presence of IC/CMB may be revealed by significant X-ray emission above 2 keV (Mernier et al. 2023), we produced 3–7 keV hard-band flux images for the five sources that show evidence of significant extended emission and present them in Figure 10, with the radio contours drawn at 3 GHz overlaid in green. We see that the only source showing significant X-ray emission in this band in correspondence with the extended radio structures is B2.1 0302+31. In particular the hard-band emission in the eastern and western radio lobes is detected at 2.4σ and 3.3σ significance. Although this is suggestive of the presence of nonthermal IC/CMB emission in this source, the low statistics do not allow us to draw firm conclusions.

The detection of this extended X-ray emission in any case suggests the presence of an ICM, indicating that these sources may belong to groups or clusters of galaxies. In the case of B2.1 0742+31, this is reinforced by the presence in the source field of five additional galaxies at a redshift close to that of the galaxy hosting B2.1 0742+31 (see Figure 11), that is, with a maximum redshift separation $\Delta z = 0.005$ (i.e., $\sim$1500 km s^{-1}) corresponding to the maximum velocity dispersion observed in groups and clusters of galaxies (see, e.g., Moore et al. 1993; Eke et al. 2004; Berlind et al. 2006). We therefore compared the properties of the hot gas surrounding these radio sources with those observed in groups and clusters of galaxies. In particular, we were interested in the hot gas X-ray luminosity versus temperature correlation (Mulchaey 2000). Since we had redshift estimates only for B2.1 0742+31 and B2.3 2254+35, we restricted our analysis to these two sources. In Figure 12 we compare the temperature (kT) and X-ray bolometric luminosity L_X of the thermal gas surrounding B2.1 0742+31 and B2.3 2254+35 with those of groups and clusters of galaxies from Figure 6 of Mulchaey (2000), where the X-ray luminosities have been rescaled to the cosmology adopted in the present analysis.

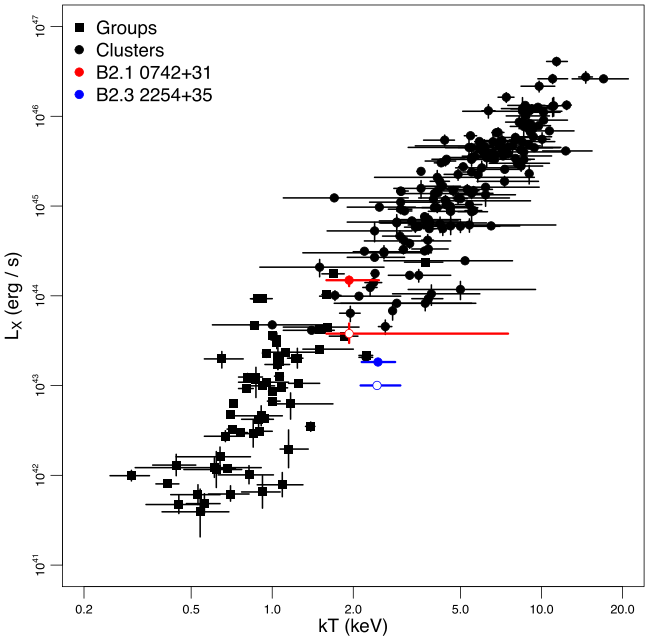

Figure 12. X-ray luminosity (L_X) vs. temperature (kT) of the X-ray-emitting plasma in groups (black squares) and clusters (black circles) of galaxies (Mulchaey 2000). Group data are from Xue & Wu (2000) and Helsdon & Ponman (2000), while data of clusters are from Wu et al. (1999). The X-ray luminosities have been rescaled to the cosmology adopted in the present analysis. In this figure we represent with red and blue circles the properties of the X-ray-emitting gas surrounding B2.1 0742+31 and B2.3 2254+35, respectively. Full colored circles indicate the results from the spectra extracted from the whole diffuse X-ray emission, while empty colored circles indicate the results from the spectra extracted from the regions that exclude the extended radio structures.

We see that, while the X-ray emission of B2.1 0742+31 is compatible with the ICM emission of low-luminosity clusters of galaxies, the X-ray diffuse emission surrounding the highly disturbed WAT B2.3 2254+35 lies somehow at the edge of the L_X–kT relation, with a luminosity similar to those of bright groups of galaxies, and a temperature similar to those of low-luminosity clusters of galaxies, possibly due to the disturbed nature of the gas surrounding this WAT.

Finally, we estimated the mass of the X-ray-emitting gas in B2.1 0742+31 and B2.3 2254+35 from the spectral fits. From the normalization of the XSAPEC models (i.e., their emission measure or EM), we can evaluate the gas proton density n_p. Assuming a uniform particle density in the emitting region, we have a proton density

$$n_p = \sqrt{\frac{10^{14}\,\mathrm{EM}\,\eta\,4\pi\,{D_A}^2(1+z)^2}{V}}, \quad (1)$$

where D_A is the angular distance of the source, V is the emitting region volume, and $\eta \approx 0.82$ is the ratio of the proton density to the electron density in a fully ionized plasma. We can estimate the total gas mass as $M_{\rm gas} = \mu m_u n_{\rm tot} V$, where m_u is the atomic mass, $n_{\rm tot} = n_p(1 + 1/\eta)$ is the total gas density, and $\mu = 0.6$ is the mean molecular weight (Ettori et al. 2013).

To estimate the volumes we modeled the projected emission regions as ellipses with semimajor and semiminor axes R and r, respectively, encompassing the diffuse X-ray and radio

[26] https://heasarc.gsfc.nasa.gov/xanadu/xspec/manual/XSmodelApec.html

emission. Then, we modeled the emitting regions as ellipsoids with volume $V = 4/3\,\pi Rr^2$ (when excluding the radio emission region, the volume would be the difference between the X-ray and radio emission region volumes; see Figure 1).

Taking into account the uncertainties on the best-fit parameters and the different spectral extraction regions (that is, regions including or excluding the extended radio structures), we estimate $M_{\rm gas} = 2.6$–$9.1 \times 10^{12}\,M_\odot$ and $M_{\rm gas} = 0.9$–$1.4 \times 10^{12}\,M_\odot$ for B2.1 0742+31 and B2.3 2254+35, respectively, typical of rich groups (see, e.g., Mulchaey 2000).

4. Summary and Conclusions

In this work we have analyzed the first 33 Chandra ACIS observations obtained through the CCT snapshot campaign on the Second Bologna Catalog of radio sources. The X-ray data have been compared with the 145 MHz LOFAR, 150 MHz GMRT, and 3 GHz VLASS data, to study the connection between the X-ray and radio emission in radio galaxies. The main results of this analysis can be summarized as follows:

1. We detected X-ray nuclear emission for 28 of the 33 sources. In particular, 19 nuclei were detected at least at 3σ significance, 7 were detected at 2σ significance, and 2 were detected with a 1σ marginal significance. For two other sources we were only able to put an upper limit on the nuclear flux, and for the remaining three sources we do not report any nuclear flux estimate, since we do not have any clear indication of the location of their core.
2. We found a mild correlation between the X-ray and radio nuclear fluxes, while the flux of diffuse X-ray emission does not appear to correlate with the radio flux of the extended radio structures.
3. Comparing the X-ray surface flux profiles of the sources with those of simulated PSFs, we detected extended emission with a minimum 5σ significance level beyond $10''$ from the nucleus in five sources.
4. We detected eight regions of increased X-ray flux in correspondence with radio hot spots or jet knots at a minimum significance level of 3σ, two of which above a 5σ level of significance. In B2.3 2254+35 we were able to detect a region of decreased flux, possibly associated with an X-ray cavity, at a 4σ level of significance.
5. We performed an X-ray spectral analysis for 15 nuclei with a power-law model, and found for the nuclei of B2.4 0004+21, B2.4 0145+22, and B2.4 0401+23 significant intrinsic absorption $N_{\rm H,int} \sim 10^{22}\,{\rm cm}^{-2}$, and for B2.4 0229+23 $N_{\rm H,int} \sim 10^{23}\,{\rm cm}^{-2}$.
6. We performed an X-ray spectral analysis of the diffuse emission surrounding three sources, finding temperatures of the hot plasma $\sim$2 keV. There is some hint of X-ray emission above 3 keV in correspondence with the radio lobes in B2.1 0302+31, which may suggest the presence of IC/CMB in this source. The low statistics however do not allow us to draw firm conclusions.
7. For two of these sources, B2.1 0742+31 and B2.3 2254+35, we compared the properties of the X-ray-emitting gas with those of the ICM surrounding clusters and groups of galaxies. While the hot gas surrounding B2.1 0742+31 is compatible with the ICM of low-luminosity clusters of galaxies, the X-ray diffuse emission surrounding the highly disturbed WAT B2.3 2254+35 features a luminosity similar to those of the ICM of bright groups of galaxies, while having a temperature similar to those of the ICM of low-luminosity clusters of galaxies. The mass of these X-ray-emitting plasmas is of the order of $\sim 10^{12}\,M_\odot$, similar to those observed in the ICM of rich groups.

These first results on the B2CAT CCT survey show that low-frequency radio selection, combined with short X-ray snapshot observations, is a powerful tool for optimizing the "fill-in" observing strategy of several X-ray telescopes. In particular, this proves to be particularly effective with the Chandra observatory, since for XMM-Newton such short observations tend to be scheduled at the end of its orbits, which are dominated by high particle background.

Acknowledgments

We thank the anonymous referee for useful comments and suggestions. This work is supported by the "Departments of Excellence 2018–2022" grant awarded by the Italian Ministry of Education, University and Research (MIUR; L. 232/2016). This research has made use of resources provided by Compagnia di San Paolo for the grant awarded to the BLENV project (S1618_L1_MASF_01) and by MIUR for the grant MASF_FFABR_17_01. A.P. acknowledges financial support from Consorzio Interuniversitario per la Fisica Spaziale (CIS) under the agreement related to the grant MASF_CONTR_FIN_18_02. F.M. acknowledges financial contribution from the agreement ASI-INAF No. 2017-14-H.0. S.E. acknowledges financial contribution from the contract ASI-INAF Athena 2019-27-HH.0, "Attività di Studio per la comunità scientifica di Astrofisica delle Alte Energie e Fisica Astroparticellare" (Accordo Attuativo ASI-INAF No. 2017-14-H.0). A.P. thanks W. R. Forman for useful comments and suggestions. This research has made use of data obtained from the Chandra Data Archive. This research has made use of software provided by the Chandra X-Ray Center (CXC) in the application packages CIAO, ChIPS, and Sherpa. This research has made use of the NASA/IPAC Extragalactic Database (https://ned.ipac.caltech.edu), which is funded by the National Aeronautics and Space Administration and operated by the California Institute of Technology. SAOImageDS9 development has been made possible by funding from the CXC, the High Energy Astrophysics Science Archive Center (HEASARC), and the JWST Mission Office at the Space Telescope Science Institute. The LOFAR data products were provided by the LOFAR Surveys Key Science Project (LSKSP; https://lofar-surveys.org/) and were derived from observations with the International LOFAR Telescope (ILT). LOFAR (van Haarlem et al. 2013) is the Low Frequency Array designed and constructed by ASTRON. It has observing, data processing, and data storage facilities in several countries, which are owned by various parties (each with its own funding sources), and which are collectively operated by the ILT Foundation under a joint scientific policy. The efforts of the LSKSP have benefited from funding from the European Research Council, NOVA, NWO, CNRS-INSU, the SURF Co-operative, the UK Science and Technology Funding Council, and the Jülich Supercomputing Centre. The authors thank the staff of the GMRT that made these observations possible. GMRT is run by the National Centre for Radio Astrophysics of the Tata Institute of Fundamental Research. The National Radio Astronomy Observatory is a facility of the National Science Foundation operated under a cooperative agreement by Associated Universities, Inc. The Pan-STARRS1 Surveys (PS1) have been made possible through contributions of

the Institute for Astronomy, the University of Hawaii, the Pan-STARRS Project Office, the Max-Planck Society and its participating institutes, the Max Planck Institute for Astronomy (Heidelberg) and the Max Planck Institute for Extraterrestrial Physics (Garching), the Johns Hopkins University, Durham University, the University of Edinburgh, Queen's University Belfast, the Harvard–Smithsonian Center for Astrophysics, the Las Cumbres Observatory Global Telescope Network Incorporated, the National Central University of Taiwan, the Space Telescope Science Institute, the National Aeronautics and Space Administration (under grant No. NNX08AR22G issued through the Planetary Science Division of the NASA Science Mission Directorate), the National Science Foundation (under grant No. AST-1238877), the University of Maryland, and Eotvos Lorand University (ELTE).

Software: CIAO (Fruscione et al. 2006), Sherpa (Freeman et al. 2001; Doe et al. 2007; Burke et al. 2023), ChiPS (Germain et al. 2006), SAOImageDS9 (Joye & Mandel 2003), TOPCAT (Taylor 2005).

Appendix
Radio Maps

In this appendix we report the available radio images for the sources considered in this work, that is, the 74 MHz VLSSr, 145 MHz LOFAR, 150 MHz TGSS, 1.4 GHz NVSS, and 3 GHz VLASS maps. The radio maps for each source are presented in Figure A1, where we overplot on the maps white dashed ellipses indicating the different radio structures, generally the two radio lobes (indicated with A and B) and radio core (indicated with N). When no radio structure is discernible, only one ellipse (indicated with A) marks the bulk emission. In Table A1 we report the specific flux estimates (in mJy) for the various structures observed in the radio maps. For each specific flux estimate we report an error that includes both the statistical and the systematic uncertainty, the latter ranging between 10% and 15% of the specific flux (e.g., Lane et al. 2014; Intema et al. 2017; Sabater et al. 2021; Krezinger et al. 2020).

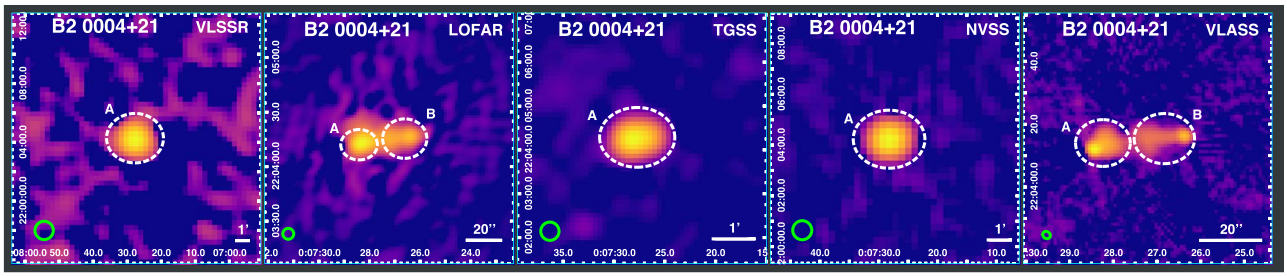

Figure A1. Radio maps for the sources considered in the present work. The white ellipses indicate the discernible radio structures, while the green ellipses on the lower left of each panel represent the FWHM restoring beam.

(The complete figure set (33 images) is available.)

Table A1
Specific Flux Estimates for the Radio Structures Indicated in Figure 13

Source Name	$F_{74\ \mathrm{MHz}}$ (mJy)			$F_{145\ \mathrm{MHz}}$ (mJy)			$F_{150\ \mathrm{MHz}}$ (mJy)			$F_{1.4\ \mathrm{GHz}}$ (mJy)			$F_{3\ \mathrm{GHz}}$ (mJy)		
	A	B	N	A	B	N	A	B	N	A	B	N	A	B	N
B2.4 0004+21	9472 ± 1579	⋯	⋯	3196 ± 320	1798 ± 180	⋯	4824 ± 731	⋯	⋯	815 ± 83	⋯	⋯	270 ± 41	125 ± 20	⋯
B2.2 0038 +25B	12,086 ± 1981	⋯	⋯	4933 ± 494	2981 ± 298	⋯	5585 ± 852	⋯	⋯	639 ± 65	⋯	⋯	127 ± 20	87 ± 14	⋯
B2.2 0143+24	4137 ± 844	⋯	⋯	896 ± 91	684 ± 69	⋯	992 ± 153	679 ± 105	⋯	187 ± 20	⋯	⋯	49 ± 8	34 ± 6	⋯
B2.4 0145+22	2796 ± 580	⋯	⋯	562 ± 57	1155 ± 116	⋯	459 ± 75	1107 ± 173	⋯	82 ± 9	195 ± 20	⋯	61 ± 10	116 ± 19	⋯
B2.4 0229+23	514 ± 242	⋯	⋯	469 ± 48	⋯	⋯	571 ± 93	⋯	⋯	459 ± 47	⋯	⋯	277 ± 42	⋯	⋯
B2.1 0241+30	6123 ± 1120	⋯	⋯	1229 ± 124	2111 ± 212	⋯	709 ± 111	1345 ± 207	⋯	173 ± 18	⋯	⋯	22 ± 4	38 ± 6	2 ± 1
B2.1 0302+31	3435 ± 698	⋯	⋯	850 ± 86	856 ± 87	⋯	1679 ± 260	⋯	⋯	373 ± 38	⋯	⋯	60 ± 10	83 ± 13	⋯
B2.4 0401+23	2529 ± 587	⋯	⋯	1179 ± 118	371 ± 37	⋯	868 ± 134	297 ± 48	⋯	198 ± 21	⋯	⋯	66 ± 10	20 ± 3	2 ± 1
B2.2 0410+26	8379 ± 1477	⋯	⋯	5335 ± 534	⋯	⋯	5286 ± 800	⋯	⋯	529 ± 54	⋯	⋯	188 ± 29	⋯	⋯
B2.4 0412+23	2566 ± 577	⋯	⋯	797 ± 80	1622 ± 163	⋯	502 ± 81	787 ± 123	⋯	276 ± 29	⋯	⋯	23 ± 4	96 ± 15	36 ± 6
B2.3 0454+35	1108 ± 509	⋯	⋯	⋯	⋯	⋯	418 ± 70	251 ± 48	⋯	97 ± 11	66 ± 7	⋯	25 ± 4	24 ± 5	9 ± 2
B2.1 0455 +32B	2185 ± 542	⋯	⋯	1355 ± 139	⋯	⋯	1639 ± 256	⋯	⋯	346 ± 36	⋯	⋯	73 ± 11	98 ± 15	⋯
B2.1 0455 +32C	5326 ± 1019	⋯	⋯	857 ± 88	1460 ± 149	⋯	3140 ± 482	⋯	⋯	561 ± 57	⋯	⋯	112 ± 17	171 ± 26	⋯
B2.3 0516+40	1246 ± 382	⋯	⋯	1325 ± 133	⋯	⋯	1700 ± 262	⋯	⋯	265 ± 28	⋯	⋯	123 ± 19	⋯	⋯
B2.1 0536 +33B	1141 ± 390	⋯	⋯	282 ± 29	535 ± 54	⋯	1129 ± 178	⋯	⋯	192 ± 20	⋯	⋯	34 ± 6	51 ± 8	5 ± 1
B2.1 0549+29	1590 ± 446	⋯	⋯	1039 ± 105	⋯	⋯	1453 ± 229	⋯	⋯	218 ± 23	⋯	⋯	50 ± 8	57 ± 9	⋯
B2.1 0643+30	570 ± 216	⋯	⋯	⋯	⋯	⋯	870 ± 144	⋯	⋯	869 ± 88	⋯	⋯	581 ± 88	⋯	⋯
B2.1 0742+31	7098 ± 1168	5018 ± 859	⋯	3718 ± 373	1818 ± 182	325 ± 33	3728 ± 569	1702 ± 263	450 ± 72	642 ± 65	475 ± 48	⋯	221 ± 35	142 ± 24	696 ± 105
B2.2 0755+24	1239 ± 364	⋯	⋯	824 ± 83	⋯	⋯	1003 ± 159	⋯	⋯	206 ± 22	⋯	⋯	53 ± 8	44 ± 7	⋯
B2.3 0848+34	2861 ± 567	⋯	⋯	2105 ± 211	⋯	⋯	⋯	⋯	⋯	341 ± 35	⋯	⋯	77 ± 12	81 ± 12	⋯
	1754 ± 404	⋯	⋯	207 ± 21	810 ± 81	⋯	1126 ± 175	⋯	⋯	207 ± 22	⋯	⋯	22 ± 4	82 ± 13	⋯

Table A1
(Continued)

Source Name	$F_{74\ \mathrm{MHz}}$ (mJy)			$F_{145\ \mathrm{MHz}}$ (mJy)			$F_{150\ \mathrm{MHz}}$ (mJy)			$F_{1.4\ \mathrm{GHz}}$ (mJy)			$F_{3\ \mathrm{GHz}}$ (mJy)		
	A	B	N	A	B	N	A	B	N	A	B	N	A	B	N
B2.4 0939 +22A															
B2.4 1112+23	2447 ± 547	⋯	⋯	1652 ± 166	⋯	⋯	1448 ± 224	⋯	⋯	375 ± 39	⋯	⋯	199 ± 30	⋯	⋯
B2.3 1234+37	9736 ± 1662	⋯	⋯	3184 ± 319	2480 ± 248	⋯	6700 ± 102	⋯	⋯	923 ± 94	⋯	⋯	262 ± 40	161 ± 25	⋯
B2.2 1334+27	2732 ± 584	⋯	⋯	2086 ± 209	257 ± 26	⋯	1390 ± 217	⋯	⋯	188 ± 20	⋯	⋯	24 ± 4	59 ± 9	⋯
B2.2 1338+27	2695 ± 588	⋯	⋯	683 ± 69	2206 ± 222	⋯	355 ± 59	1139 ± 176	⋯	51 ± 6	120 ± 13	⋯	19 ± 3	49 ± 8	⋯
B2.2 1439+25	655 ± 230	1074 ± 309	⋯	403 ± 41	755 ± 76	⋯	319 ± 59	707 ± 118	⋯	73 ± 8	132 ± 14	⋯	40 ± 7	70 ± 12	⋯
B2.4 1512+23	1280 ± 424	⋯	⋯	319 ± 33	365 ± 37	⋯	261 ± 45	278 ± 48	⋯	241 ± 25	⋯	⋯	58 ± 10	60 ± 10	3 ± 1
B2.4 2054 +22B	1928 ± 485	⋯	⋯	⋯	⋯	⋯	1238 ± 196	⋯	⋯	194 ± 21	⋯	⋯	47 ± 8	46 ± 7	⋯
B2.2 2104+24	6928 ± 1232	⋯	⋯	2112 ± 217	794 ± 84	⋯	3466 ± 532	⋯	⋯	501 ± 51	⋯	⋯	144 ± 22	50 ± 8	17 ± 3
B2.2 2133+27	3760 ± 744	⋯	⋯	1746 ± 179	⋯	⋯	1447 ± 224	⋯	⋯	281 ± 29	⋯	⋯	72 ± 12	47 ± 8	⋯
B2.3 2254+35	5701 ± 1138	⋯	⋯	1304 ± 131	1911 ± 193	⋯	852 ± 140	1182 ± 202	⋯	492 ± 51	⋯	⋯	78 ± 13	117 ± 19	2 ± 1
B2.2 2328+26	2860 ± 650	⋯	⋯	1790 ± 179	⋯	⋯	1508 ± 235	⋯	⋯	413 ± 42	⋯	⋯	210 ± 32	⋯	⋯
B2.3 2334+39	2747 ± 592	⋯	⋯	917 ± 94	697 ± 72	119 ± 12	815 ± 130	719 ± 117	⋯	469 ± 48	⋯	⋯	102 ± 18	76 ± 14	9 ± 2

Notes. In particular, $F_{74\ \mathrm{MHz}}$ represents the VLSSr flux, $F_{145\ \mathrm{MHz}}$ the LOFAR flux, $F_{150\ \mathrm{MHz}}$ the TGSS flux, $F_{1.4\ \mathrm{GHz}}$ the NVSS flux, and $F_{3\ \mathrm{GHz}}$ the VLASS flux. The quoted errors include both the statistical and the systematic uncertainty.

ORCID iDs

A. Paggi https://orcid.org/0000-0002-5646-2410
F. Massaro https://orcid.org/0000-0002-1704-9850
H. Penã-Herazo https://orcid.org/0000-0003-0032-9538
V. Missaglia https://orcid.org/0000-0001-8382-3229
A. Jimenez-Gallardo https://orcid.org/0000-0003-4413-7722
F. Ricci https://orcid.org/0000-0001-5742-5980
S. Ettori https://orcid.org/0000-0003-4117-8617
G. Giovannini https://orcid.org/0000-0003-4916-6362
F. Govoni https://orcid.org/0000-0003-3644-3084
R. D. Baldi https://orcid.org/0000-0002-1824-0411
B. Mingo https://orcid.org/0000-0001-5649-938X
M. Murgia https://orcid.org/0000-0002-4800-0806
E. Liuzzo https://orcid.org/0000-0003-0995-5201

References

Ahn, C. P., Alexandroff, R., Allende Prieto, C., et al. 2012, ApJS, 203, 21
Alam, S., Albareti, F. D., Allende Prieto, C., et al. 2015, ApJS, 219, 12
Balmaverde, B., Capetti, A., Grandi, P., et al. 2012, A&A, 545, A143
Belsole, E., Worrall, D. M., Hardcastle, M. J., et al. 2007, MNRAS, 381, 1109
Bennett, A. S. 1962, MNRAS, 125, 75
Bennett, C. L., Larson, D., Weiland, J. L., et al. 2014, ApJ, 794, 135
Bergamini, R., Londrillo, P., & Setti, G. 1967, NCimB, 52, 495
Berlind, A. A., Frieman, J., Weinberg, D. H., et al. 2006, ApJS, 167, 1
Bilicki, M., Jarrett, T. H., Peacock, J. A., Cluver, M. E., & Steward, L. 2014, ApJS, 210, 9
Breiding, P., Meyer, E. T., Georganopoulos, M., et al. 2023, MNRAS, 518, 3222
Brinkmann, W., Laurent-Muehleisen, S. A., Voges, W., et al. 2000, A&A, 356, 445
Brinkmann, W., Yuan, W., & Siebert, J. 1997, A&A, 319, 413
Burke, D., Laurino, O., Wmclaugh, et al. 2023, sherpa/sherpa: Sherpa 4.15.1, v4.15.1, Zenodo, doi:10.5281/zenodo.7948720
Capetti, A., Celotti, A., Chiaberge, M., et al. 2002, A&A, 383, 104
Chambers, K. C., Magnier, E. A., Metcalfe, N., et al. 2016, arXiv:1612.05560
Colla, G., Fanti, C., Fanti, R., et al. 1972, A&AS, 7, 1
Colla, G., Fanti, C., Fanti, R., et al. 1973, A&AS, 11, 291
Colla, G., Fanti, C., Ficarra, A., et al. 1970, A&AS, 1, 281
Condon, J. J., Cotton, W. D., Greisen, E. W., et al. 1998, AJ, 115, 1693
Crawford, C. S., & Fabian, A. C. 2003, MNRAS, 339, 1163
Dasadia, S., Sun, M., Morandi, A., et al. 2016, MNRAS, 458, 681
Davis, J. E. 2001, ApJ, 562, 575
de Ruiter, H. R., Parma, P., Capetti, A., et al. 2002, A&A, 396, 857
Doe, S., Nguyen, D., Stawarz, C., et al. 2007, in ASP Conf. Ser. 376, Astronomical Data Analysis Software and Systems XVI, ed. R. A. Shaw, F. Hill, & D. J. Bell (San Francisco, CA: ASP), 543
Eke, V. R., Baugh, C. M., Cole, S., et al. 2004, MNRAS, 348, 866
Erlund, M. C., Fabian, A. C., Blundell, K. M., et al. 2006, MNRAS, 371, 29
Ettori, S., Donnarumma, A., Pointecouteau, E., et al. 2013, SSRv, 177, 119
Evans, D. A., Worrall, D. M., Hardcastle, M. J., et al. 2006, ApJ, 642, 96
Fabbiano, G., Paggi, A., Karovska, M., et al. 2020, ApJ, 902, 49
Fabian, A. C. 2012, ARA&A, 50, 455
Fabian, A. C., Crawford, C. S., Ettori, S., et al. 2001, MNRAS, 322, L11
Fabian, A. C., Sanders, J. S., Crawford, C. S., et al. 2003, MNRAS, 341, 729
Fanaroff, B. L., & Riley, J. M. 1974, MNRAS, 167, 31P
Fanti, C., Fanti, R., de Ruiter, H. R., et al. 1987, A&AS, 69, 57
Fanti, C., Fanti, R., Ficarra, A., et al. 1974, A&AS, 18, 147
Fanti, R., Ficarra, A., Formiggini, L., et al. 1974, A&A, 32, 155
Freeman, P., Doe, S., & Siemiginowska, A. 2001, Proc. SPIE, 4477, 76
Fruscione, A., McDowell, J. C., Allen, G. E., et al. 2006, Proc. SPIE, 6270, 62701V
Garon, A. F., Rudnick, L., Wong, O. I., et al. 2019, AJ, 157, 126
Germain, G., Milaszewski, R., McLaughlin, W., et al. 2006, in ASP Conf. Ser. 351, Astronomical Data Analysis Software and Systems XV, ed. C. Gabriel et al. (San Francisco, CA: ASP), 57
Gioia, I. M., & Gregorini, L. 1980, A&AS, 41, 329
Gobat, R., Daddi, E., Onodera, M., et al. 2011, A&A, 526, A133
Golden-Marx, E., Blanton, E. L., Paterno-Mahler, R., et al. 2021, ApJ, 907, 65
Gopal-Krishna, & Wiita, P. J. 2000, A&A, 363, 507
Gursky, H., Kellogg, E., Murray, S., et al. 1971, ApJL, 167, L81
Hardcastle, M. J., Evans, D. A., & Croston, J. H. 2006, MNRAS, 370, 1893
Hardcastle, M. J., Evans, D. A., & Croston, J. H. 2009, MNRAS, 396, 1929
Hardcastle, M. J., Harris, D. E., Worrall, D. M., et al. 2004, ApJ, 612, 729
Hardcastle, M. J., Massaro, F., & Harris, D. E. 2010, MNRAS, 401, 2697
Hardcastle, M. J., Massaro, F., Harris, D. E., et al. 2012, MNRAS, 424, 1774
Harris, D. E., & Grindlay, J. E. 1979, MNRAS, 188, 25
Harris, D. E., Lari, C., Vallee, J. P., et al. 1980, A&AS, 42, 319
Helsdon, S. F., & Ponman, T. J. 2000, MNRAS, 315, 356
Hoyle, F. 1965, Natur, 208, 111
HI4PI Collaboration, Ben Bekhti, N., Flöer, L., et al. 2016, A&A, 594, A116
Ineson, J., Croston, J. H., Hardcastle, M. J., et al. 2013, ApJ, 770, 136
Ineson, J., Croston, J. H., Hardcastle, M. J., et al. 2015, MNRAS, 453, 2682
Intema, H. T., Jagannathan, P., Mooley, K. P., et al. 2017, A&A, 598, A78
Jimenez-Gallardo, A., Massaro, F., Paggi, A., et al. 2021, ApJS, 252, 31
Jimenez-Gallardo, A., Massaro, F., Prieto, M. A., et al. 2020, ApJS, 250, 7
Jimenez-Gallardo, A., Sani, E., Ricci, F., et al. 2022, ApJ, 941, 114
Jones, C., Mandel, E., Schwarz, J., et al. 1979, ApJL, 234, L21
Joye, W. A., & Mandel, E. 2003, in ASP Conf. Ser. 295, Astronomical Data Analysis Software and Systems XII, ed. H. E. Payne, R. I. Jedrzejewski, & R. N. Hook (San Francisco, CA: ASP), 489
Kaastra, J. S. 1992, An X-Ray Spectral Code for Optically Thin Plasmas, Internal SRON-Leiden Report (updated version 2.0)
Kataoka, J., & Stawarz, Ł. 2005, ApJ, 622, 797
Kelly, B. C. 2007, ApJ, 665, 1489
Kerr, F. J., & Lynden-Bell, D. 1986, MNRAS, 221, 1023
Kraft, R. P., Birkinshaw, M., Nulsen, P. E. J., et al. 2012, ApJ, 749, 19
Krezinger, M., Frey, S., Paragi, Z., et al. 2020, Symmetry, 12, 527
Lacy, M., Baum, S. A., Chandler, C. J., et al. 2020, PASP, 132, 035001
Lane, W. M., Cotton, W. D., van Velzen, S., et al. 2014, MNRAS, 440, 327
Law-Green, J. D. B., Leahy, J. P., Alexander, P., et al. 1995, MNRAS, 274, 939
Leahy, J. P. 1993, in Jets in Extragalactic Radio Sources, ed. H.-J. Röser & K. Meisenheimer (Berlin: Springer), 1
Mannering, E., Worrall, D. M., & Birkinshaw, M. 2013, MNRAS, 431, 858
Markevitch, M., Bautz, M. W., Biller, B., et al. 2003, ApJ, 583, 70
Maselli, A., Kraft, R. P., Massaro, F., et al. 2018, A&A, 619, A75
Massaro, F., Chiaberge, M., Grandi, P., et al. 2009, ApJL, 692, L123
Massaro, F., Harris, D. E., & Cheung, C. C. 2011, ApJS, 197, 24
Massaro, F., Harris, D. E., Chiaberge, M., et al. 2009, ApJ, 696, 980
Massaro, F., Harris, D. E., Liuzzo, E., et al. 2015, ApJS, 220, 5
Massaro, F., Harris, D. E., Tremblay, G. R., et al. 2010, ApJ, 714, 589
Massaro, F., Harris, D. E., Tremblay, G. R., et al. 2013, ApJS, 206, 7
Massaro, F., Missaglia, V., Stuardi, C., et al. 2018, ApJS, 234, 7
Massaro, F., Tremblay, G. R., Harris, D. E., et al. 2012, ApJS, 203, 31
Mernier, F., Werner, N., Bagchi, J., et al. 2023, MNRAS, 524, 4939
Meyer, E. T., Iyer, A. R., Reddy, K., et al. 2019, ApJL, 883, L2
Mingo, B., Hardcastle, M. J., Croston, J. H., et al. 2014, MNRAS, 440, 269
Mingo, B., Hardcastle, M. J., Ineson, J., et al. 2017, MNRAS, 470, 2762
Missaglia, V., Massaro, F., Capetti, A., et al. 2019, A&A, 626, A8
Missaglia, V., Massaro, F., Liuzzo, E., et al. 2021, ApJS, 255, 18
Moore, B., Frenk, C. S., & White, S. D. M. 1993, MNRAS, 261, 827
Mulchaey, J. S. 2000, ARA&A, 38, 289
Okoye, S. E. 1972, MNRAS, 160, 339
Okoye, S. E. 1973, MNRAS, 165, 413
Orienti, M., Prieto, M. A., Brunetti, G., et al. 2012, MNRAS, 419, 2338
Owen, F. N., & Rudnick, L. 1976, ApJL, 205, L1
Padrielli, L., Kapahi, V. K., & Katgert-Merkelijn, J. K. 1981, A&AS, 46, 473
Paggi, A., Massaro, F., Peña-Herazo, H. A., et al. 2021, A&A, 647, A79
Parekh, V., Dwarakanath, K. S., Kale, R., et al. 2017, MNRAS, 464, 2752
Ricci, F., Lovisari, L., Kraft, R. P., et al. 2018, ApJ, 867, 35
Rogora, A., Padrielli, L., & de Ruiter, H. R. 1986, A&AS, 64, 557
Sabater, J., Best, P. N., Tasse, C., et al. 2021, A&A, 648, A2
Saripalli, L., & Roberts, D. H. 2018, ApJ, 852, 48
Scharf, C., Smail, I., Ivison, R., et al. 2003, ApJ, 596, 105
Schwartz, D. A., Marshall, H. L., Lovell, J. E. J., et al. 2000, ApJL, 540, L69
Shimwell, T. W., Hardcastle, M. J., Tasse, C., et al. 2022, A&A, 659, A1
Shimwell, T. W., Röttgering, H. J. A., Best, P. N., et al. 2017, A&A, 598, A104
Shimwell, T. W., Tasse, C., Hardcastle, M. J., et al. 2019, A&A, 622, A1
Smail, I., Blundell, K. M., Lehmer, B. D., et al. 2012, ApJ, 760, 132
Smail, I., Lehmer, B. D., Ivison, R. J., et al. 2009, ApJL, 702, L114
Snellen, I. A. G., McMahon, R. G., Hook, I. M., et al. 2002, MNRAS, 329, 700
Spinrad, H., Djorgovski, S., Marr, J., et al. 1985, PASP, 97, 932
Stuardi, C., Missaglia, V., Massaro, F., et al. 2018, ApJS, 235, 32
Tasse, C., Shimwell, T., Hardcastle, M. J., et al. 2021, A&A, 648, A1
Tavecchio, F., Maraschi, L., Sambruna, R. M., et al. 2000, ApJL, 544, L23

Taylor, M. B. 2005, in ASP Conf. Ser. 347, Astronomical Data Analysis Software and Systems XIV, ed. P. Shopbell, M. Britton, & R. Ebert (San Francisco, CA: ASP), 29
van Haarlem, M. P., Wise, M. W., Gunst, A. W., et al. 2013, A&A, 556, A2
van Weeren, R. J., de Gasperin, F., Akamatsu, H., et al. 2019, SSRv, 215, 16
Voges, W., Aschenbach, B., Boller, T., et al. 1999, A&A, 349, 389
Worrall, D. M. 2002, NewAR, 46, 121
Worrall, D. M. 2009, A&ARv, 17, 1
Worrall, D. M., & Birkinshaw, M. 1994, ApJ, 427, 134
Wu, X.-P., Xue, Y.-J., & Fang, L.-Z. 1999, ApJ, 524, 22
Xue, Y.-J., & Wu, X.-P. 2000, ApJ, 538, 65
Zuther, J., Fischer, S., & Eckart, A. 2012, A&A, 543, A57